

UCSF

UC San Francisco Previously Published Works

Title

Single-cell spatial proteomic imaging for human neuropathology.

Permalink

<https://escholarship.org/uc/item/4h59336x>

Journal

Acta Neuropathologica Communications, 10(1)

Authors

Vijayaragavan, Kausalia

Cannon, Bryan

Tebaykin, Dmitry

et al.

Publication Date

2022-11-04

DOI

10.1186/s40478-022-01465-x


Peer reviewed

METHODOLOGY ARTICLE

Open Access



Single-cell spatial proteomic imaging for human neuropathology

Kausalia Vijayaragavan^{1†}, Bryan J. Cannon^{1†}, Dmitry Tebaykin¹, Marc Bossé¹, Alex Baranski¹, J. P. Oliveria¹, Syed A. Bukhari¹, Dunja Mrdjen¹, M. Ryan Corces³, Erin F. McCaffrey¹, Noah F. Greenwald¹, Yari Sigal², Diana Marquez¹, Zumana Khair¹, Trevor Bruce¹, Mako Goldston¹, Anusha Bharadwaj¹, Kathleen S. Montine¹, R. Michael Angelo¹, Thomas J. Montine¹ and Sean C. Bendall^{1*} 

Abstract:

Neurodegenerative disorders are characterized by phenotypic changes and hallmark proteopathies. Quantifying these in archival human brain tissues remains indispensable for validating animal models and understanding disease mechanisms. We present a framework for nanometer-scale, spatial proteomics with multiplex ion beam imaging (MIBI) for capturing neuropathological features. MIBI facilitated simultaneous, quantitative imaging of 36 proteins on archival human hippocampus from individuals spanning cognitively normal to dementia. Customized analysis strategies identified cell types and proteopathies in the hippocampus across stages of Alzheimer's disease (AD) neuropathologic change. We show microglia-pathologic tau interactions in hippocampal CA1 subfield in AD dementia. Data driven, sample independent creation of spatial proteomic regions identified persistent neurons in pathologic tau neighborhoods expressing mitochondrial protein MFN2, regardless of cognitive status, suggesting a survival advantage. Our study revealed unique insights from multiplexed imaging and data-driven approaches for neuropathologic analysis and serves broadly as a methodology for spatial proteomic analysis of archival human neuropathology.

Teaser: Multiplex Ion beam Imaging enables deep spatial phenotyping of human neuropathology-associated cellular and disease features.

Introduction

Neurodegenerative diseases are a heterogeneous group of disorders characterized by progressive dysfunction and loss of neurons, usually alongside aberrant protein accumulation. These proteopathies are accompanied by microglia [1, 2] and astrocyte [3] stress responses and neurovascular dysfunction and occur in characteristic brain regions that underlie clinical symptoms of disease. Alzheimer's Disease (AD), the most common

neurodegenerative disease, portrays these features. In AD, aggregation of amyloid- β (A β) peptides in parenchymal space as plaques and hyperphosphorylated, paired-helical filament (PHF) tau as intraneuronal neurofibrillary tangles (NFTs) and neuropil threads (NTs) form region-specific niches of neurodegeneration. Pathologic aggregates of PHF tau accumulate first in the entorhinal cortex and hippocampus; A β plaques deposit first across neocortical regions [4, 5].

Our understanding of the underlying phenotypic, regional, and cellular heterogeneity in neurodegenerative niches of these vulnerable brain regions remains limited [6]. Capturing discrete cellular and proteopathy features could be used to calculate local and regional tissue neighborhoods and their relationship to neurodegenerative disease progression. Quantitative, multiplexed,

[†]Kausalia Vijayaragavan and Bryan J. Cannon contributed equally to this work

*Correspondence: bendall@stanford.edu

¹ Department of Pathology, School of Medicine, Stanford University, Stanford, CA, USA

Full list of author information is available at the end of the article



© The Author(s) 2022. **Open Access** This article is licensed under a Creative Commons Attribution 4.0 International License, which permits use, sharing, adaptation, distribution and reproduction in any medium or format, as long as you give appropriate credit to the original author(s) and the source, provide a link to the Creative Commons licence, and indicate if changes were made. The images or other third party material in this article are included in the article's Creative Commons licence, unless indicated otherwise in a credit line to the material. If material is not included in the article's Creative Commons licence and your intended use is not permitted by statutory regulation or exceeds the permitted use, you will need to obtain permission directly from the copyright holder. To view a copy of this licence, visit <http://creativecommons.org/licenses/by/4.0/>. The Creative Commons Public Domain Dedication waiver (<http://creativecommons.org/publicdomain/zero/1.0/>) applies to the data made available in this article, unless otherwise stated in a credit line to the data.

subcellular imaging of cells and biochemical components may connect these various domains. Such subcellular mapping has been shown using immunofluorescence within in vitro systems [7]. However, efforts to acquire highly multiplexed fluorescence-based images have been confounded by the variable auto-fluorescent matrix common to aged human brain formalin fixed paraffin embedded (FFPE) samples [8, 9]. Furthermore, the ramified morphology of glia and neurons present significant analytical challenges to conventional methods for image segmentation and interpretation [10]. Partitioning disjointed, unusually shaped or sized cellular features, acellular protein aggregates, and unclear tissue boundaries requires a specific set of analytical tools [11].

Here, we present a new generation of single-cell, spatial proteomic imaging, and analytical tools to capture the underlying cellular and phenotypic diversity in intricate neural tissues. In place of fluorophores and lasers, we employed multiplex ion beam imaging by time of flight (MIBI-TOF) mass spectrometry (MS) that has been used previously to study various archival human tissue types from tumors to placenta and granulomas in infectious disease [10, 12–15]. MIBI-TOF assay and data imaging is also highly concordant with standard single-plex IHC [16]. Based on secondary ion mass spectrometry (SIMS), MIBI-TOF images antigens targeted by antibodies labeled with elemental isotopic mass reporters that are spatially quantified with nanometer resolution. This MS-based strategy bypasses the light-based imaging matrix effects and autofluorescence that dominate in adult human CNS. Through verification against traditional IHC, we validated antibodies for 39 brain-specific targets (Additional file 1: Table S1) and demonstrate these could be simultaneously stained and imaged with MIBI-TOF without the need for cyclic or serial approaches (see for comprehensive review of [17]). A 36-plex brain-abundant targets were used for subsequent quantitative, multiplexed, spatial proteomic profiling across different brain regions, normative and AD hippocampus. We were able to employ data-driven approaches to organize brain regions independently of local anatomy and AD disease status.

Finally, as a proof-of-utility for this methodological resource, we used archival human hippocampus from individuals covering a spectrum of cognitive impairment and AD neuropathologic changes. Adapting tools for automated feature identification, we extracted and classified a wide range of brain cellular features and proteopathies. These were then combined to create tailored spatial analysis approaches, identifying organization within hippocampal subfields [10, 18]. Traditional single-cell data clustering, spatial correlation, and dimensionality reduction were used to reveal salient features. *Top-down*

analysis, (leveraging prior knowledge of neuroanatomy), as well as *bottom-up* (completely data driven) approaches established complex spatial phenotypes across 275,808 cells and anatomical objects. Top-down analysis demonstrated changes in cellular composition across pathological stages related to AD progression, such as active microglia phenotypes in hippocampal subfield CA1 as evidenced by relatively high levels of Iba1, CD45, APOE, and CD33. Bottom-up analysis identified novel cellular neighborhoods with unique neuronal populations. Most interestingly, a pathologic Tau region present in the hippocampus of all individuals, regardless of cognitive status, showed a subset of persistent, pathologic protein free neurons expressing higher levels of the mitochondrial protein MFN2. These insights were uniquely revealed by our multiplexed imaging and data-driving approaches tailored here for neuropathology research. Taken together, we provide an approach for acquisition, processing, and interpretation of highly multiplexed imaging of archival human brain tissue by MIBI-TOF.

Results

A framework for quantitative multiplexed imaging and feature selection in human brain

Archival, formalin fixed paraffin embedded (FFPE) brain regions are predominantly used for human neurodegenerative disease research. Fluorescence imaging on adult brain FFPE is confounded by endogenous tissue autofluorescence that can overwhelm signals originating from antibody bound fluorophores (Additional file 1: Fig. S1A) [8, 9, 19]. With this in mind, we created a framework for high resolution, quantitative, multiplexed imaging of archival brain regions (Fig. 1a) using MIBI-TOF. Because antibodies are detected using elemental mass tags, MIBI-TOF images possess no equivalent endogenous signal from the biological matrix (i.e., no equivalent 'autofluorescence'). Brain tissue sections were stained with a cocktail of primary antibodies (36-plex panel), where each antibody is labeled with a unique elemental mass tag (Fig. 1a, Additional file 1: Fig. S1B, Table S1). Stained brain sections were imaged using an ion beam, which liberates these mass reporters as secondary ions (Fig. 1a). The spatial distribution of elemental reporters is converted into an N -dimensional image where each channel of this image corresponds to one of the primary antibodies (Fig. 1a). Quantitative pixel-level information was extracted to produce global expression summaries and fed into downstream pipelines for data-driven analysis of cell phenotypes and protein aggregate classification (see Methods: *Global expression pattern*) [10]. Ultimately, these data were used to construct tabular summaries of molecular features describing overall tissue architecture,

as well as the spatial distribution of cells and proteopathies (Fig. 1a).

To capture salient neuropathologic changes, the antibody staining panel targeted proteins for delineating major neuronal cell lineages, proteopathies, and vascular structures (Additional file 1: Fig. S1B, Table S1). Antibody specificities were validated against multiple brain regions by standard single-plex IHC (Additional file 1: Fig. S1C), benchmarking optimal titers and emphasizing the concordance of chromogenic IHC with MIBI-TOF imaging, like seen on our previous validation study with multiple other tissue organs [16]. MIBI spectral images may not completely recapitulate the visual features of IHC, due to the differences in chromogenic light capturing vs quantitative ion count-based construction of MIBI images. Particularly, in this study we only scanned a single depth of 100–300 nm tissue [16, 20]. Thus, cell type markers which meander in CNS tissue, such as Iba1, may have been partially captured from the 5 μm thick FFPE tissue. However, given we are capturing a large area of tissue in the x and y domains these markers still give valuable information about how different cell types interact locally. We used the resulting 36-plex panel to reveal the cytoarchitecture of an entire coronal section of human hippocampus (Fig. 1b–e). Hippocampus consists of anatomically distinct regions with structural boundaries that are evident from pseudo-colored overlays. Figure 1b–e illustrates a 31 mm^2 hippocampal region from a person with AD dementia (ADD, Additional file 1: Table S2B). The granule cell layer of dentate gyrus (DG) is highlighted by MAP2 and HH3 (Fig. 1b, DG *white arrow*), while the boundary between white and gray matter can be delineated based on expression of MBP and CD56 (Fig. 1b). In line with previous work, glutamatergic terminals within the hilus, Cornu Ammonis (CA), and molecular layers (Lmol) are marked by the presynaptic vesicular proteins VGLUT1 and VGLUT2 (Fig. 1b) [21–23]. Calbindin (CB), calretinin (CR), and parvalbumin (PV) appear as contiguous parcels in the hippocampus (Fig. 1d). As seen in rat hippocampus [23], our human data showed that CB borders the DG and hilus, CR structures the Lmol, and PV is within CA4-CA1 [24]. As expected, NFTs and

NFTs are highlighted by PHF1-TAU immunoreactivity in the CA1 subfield, while A β plaques depicted by A β 42-immunoreactivity predominantly in hilus and Lmol of the ADD hippocampus (Fig. 1e). Spectral images of all simultaneously acquired markers are illustrated in Additional file 1: Fig. S4I. Taken together, this comprehensive survey of brain phenotypes highlights the capability of our approach to visualize multiplexed signatures that reveal salient structural hallmarks and proteopathies in human hippocampus.

Multiplex imaging protein signatures organize anatomical structures

Given the visual differences in expression across hippocampus subfields, we next sought to validate the strength of the 36-plex panel in a quantifiable manner across a broader set of brain regions (Fig. 2). We used the 36-plex panel to analyze a tissue microarray (TMA) containing six different brain regions from cognitively normal individuals (Fig. 2a; Additional file 1: Table S2A). A total of 24 FOVs (4 per brain region) was acquired at low-resolution scan resolving $\sim 1 \mu\text{m}^2/\text{pixel}$. A subset of markers (25-plex), namely phenotypic and structural targets, was selected for unsupervised clustering of the FOVs and markers. Firstly, except for medulla oblongata (MO), unsupervised clustering organized the different FOVs into similar anatomical brain regions (Fig. 2b). Secondly, mean pixel intensity z-score heatmap shows that many markers exhibited noticeable gradients that are consistent with canonical brain region compositions. For instance, calcium-binding proteins (PV, CB, and CR), that play important roles in memory processes, show laminar distributions and densities within and across the brain regions (Fig. 2b, c). These patterns look like published protein and gene expression profiles in mouse, rat and human, [25–27]. Notably within the cerebellum cluster, we observed an enrichment of CB with inhibitory VGAT, and CR with excitatory VGLUT2 markers possible highlighting presence of Purkinje cells in concordance previous reports on human and non-human primate cerebellum (Fig. 2b, c) [28, 29]. Likewise, TH and GAD65/67 are enriched in FOVs for SN and LC marking

(See figure on next page.)

Fig. 1 Workflow and Features Extracted from MIBI-TOF Spectral Images. **a** MIBI-TOF experimental workflow begins with the staining of FFPE brain regions (e.g., hippocampus, substantia nigra, striatum, locus coeruleus, medulla oblongata, cerebellum) on conductive gold sides, and imaging with a panel of 36 antibodies, each labeled with a unique elemental mass tag. Stained tissue sections were rasterized and resulted in a 36-dimensional image revealing protein expression at unique spatial coordinates in a selected field of view (FOV). MIBI-TOF generates data to quantify and visualize tissue architecture, which allows analysis of global protein expression and distribution, discretization into biological units for exploring marker relationships within the biological units, and investigation of distance relationships and neighborhoods among these biological units. **b–e** Montage of 196 tiled FOVs MIBI-TOF image from a post-mortem FFPE archival human hippocampus from an individual with AD dementia (ADD). Each tile is a $500\mu\text{m}^2$ spectral image acquired at low-resolution scan resolving $\sim 1 \mu\text{m}^2/\text{pixel}$. Representative 11 out of 36 spectral images were pseudo-colored and overlaid to show the spatial distribution and expression of structural and molecular markers. Abbreviations: DG, Dentate Gyrus; CA, Conus Ammonis; Lmol, molecular layer

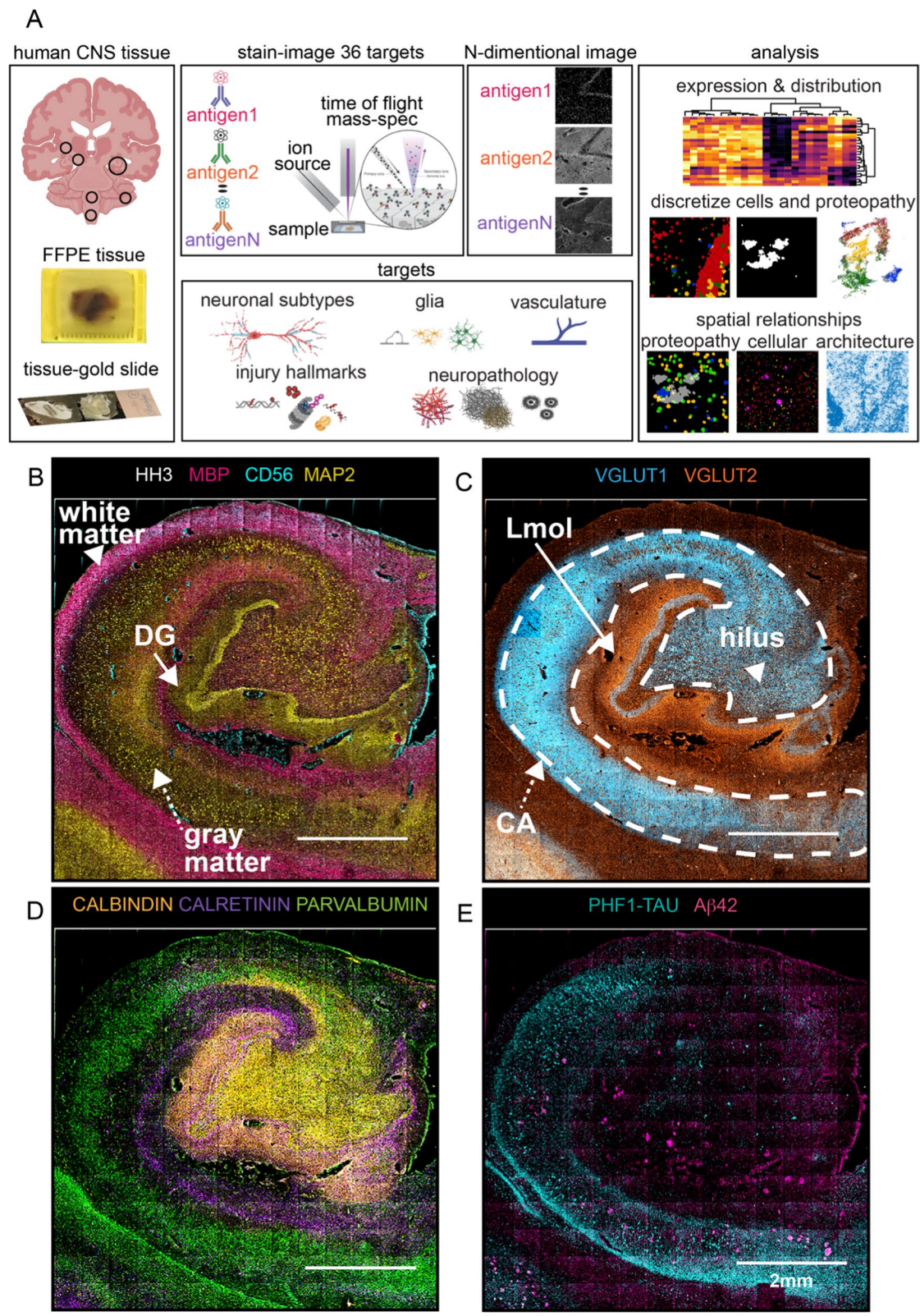


Fig. 1 (See legend on previous page.)

presence of dopaminergic neurons (Fig. 2b, d). The lower z-scores across most markers of the CA1 brain region can be explained by rarefaction of neuropil in the TMA core. Furthermore, FOVs from tissue sample of a cognitive impaired individual (CA1-ADD, CA1-AD dementia) were grouped in an unsupervised manner from normative (CA1), with these 25-plex phenotypic and structural targets (Additional file 1: Figs. S2B, S2C). Suggesting, cytoarchitectural alterations (Additional file 1: Fig. S2B), apart from gain of pan AD disease markers like PHF1/Tau and A β , in the CA1-ADD tissue sampled (Additional file 1: Fig. S2C). Altogether, much like multiplexed analysis of the immune system and other tissues [10, 13, 15, 30–33], combinatorial protein expression patterns provided a snapshot of functional organization or proteopathy within brain regions. This low-level analysis of multiplexed proteomic data could serve as a guide for ‘fingerprinting’ human brain and be used to model progression in neurodegeneration.

Discretized cellular and pathological features identify lineage and disease pathology-specific subclusters

We next discretized cells and proteopathies as biological units: neurons, astrocytes, microglia, vasculature, tau neurofibrillary tangles-neuropil threads (NFT-NTs), and A β plaques. Segmentation of planar brain tissue sections has inherent problems due to shape, texture, the disjointed features from neuronal and glial processes in the tissue section, but distant from their cell bodies, and from nonconforming shapes defining protein aggregates. As shown in Fig. 3a (*dashed lines*), we observed these various facets of planar imaging by both standard IHC and MIBI-TOF. To capture these attributes, two segmentation methods were used to partition neuronal perikaryons, microglia, astrocytes, and their processes, endothelial and their vascular-boundaries, A β plaques, and NFT-NTs (Fig. 3b). An adapted version of DeepCell was used for nuclear segmentation (Fig. 3b) [34–36]. For features not associated with nuclei, a pixel intensity thresholding-based method was used to partition cell

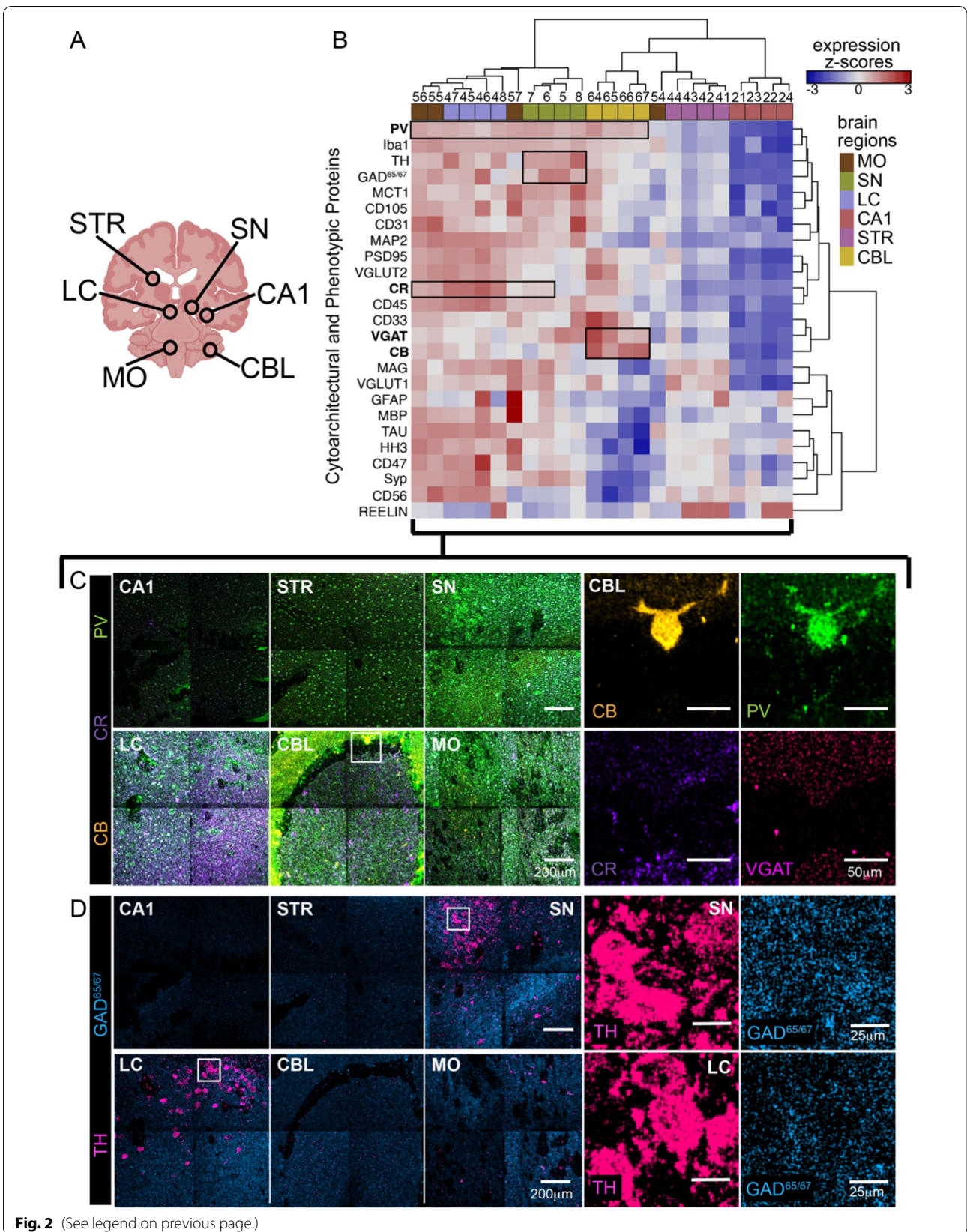
body microglial and astrocyte projections, larger vascular structures, A β plaques, and NFT-NTs (Fig. 3b, see Methods: *Object segmentation*).

The same 36-plex stain of ADD hippocampus from Fig. 1b was chosen for the discretization analysis to capture a greater breadth of morphological and pathological landscapes. With nuclear segmentation, we identified 15,270 nuclei-associated cells across 85 connected imaging FOVs which were classified using manual gating (Additional file 1: Table S4, see Methods: *Manual gating ADD hippocampus*). With the pixel-based approach, we identified 19,332 features not associated with nuclei that included microglia, astrocytes, endothelial cells, A β plaques, and NFT-NTs (Additional file 1: Table S4). Neuron masks identified by nuclear segmentation were integrated with masks of the object segmented data (microglia, astrocytes, vasculature, A β plaques, and NFTs-NTs) to obtain a comprehensive repertoire of neuronal and non-neuronal cell types as well as disease features. We then generated a UMAP [37] plot organized by lineage and proteopathy markers to analyze the relationship between these features (*see Methods: 1024 × 1024 ADD Images*). Extracted cellular and proteopathy features mapped to four cell-type clusters (neurons, microglia, astrocytes, and vasculature) and two pathologic component clusters (A β plaques and NFTs-NTs) (Fig. 3d, inset).

NFT-NT masks (cyan) mostly interrelated with the neuron (dark red) cloud (Fig. 3d, Additional file 1: Fig. S3K). This is consistent with known accrual of NFT-NTs in intraneuronal compartments [6, 38]. A β plaques shared the UMAP space mainly with astrocyte (dark green, Fig. 3d, Additional file 1: Fig. S3L) and neuronal populations (Fig. 3d, Additional file 1: S3M) as well as scattered with microglia (dark yellow) and vascular groups (Fig. 3d). In accordance with previous reports, both astrocytes and neurons highly express A β , and GFAP(+) reactive astrocytes accumulate A β in the process of clearance in AD [39–41].

(See figure on next page.)

Fig. 2 Global phenotypic expression organizes CNS sub-regions in a data driven manner. **a** Schematic of brain regions used in construction of TMA; circle highlights 3 mm cores isolated from FFPE tissues. The photomicrograph of the brain TMA cores stained with Luxol Fast Blue/Hematoxylin and Eosin (LFB/H&E) and the rastered areas, highlighted in black boxes, are shown in Additional file 1: Fig. S2A. **b** Heatmap of mean z-score distribution of pixel expression of proteins per rastered FOV (row normalized). Columns and rows are hierarchically clustered (Euclidean distance). Variance between and among FOVs are stratified in an unsupervised manner into similar anatomical regions. Black boxes highlight distribution of different calcium binding proteins, PV predominantly expression in cerebellum, midbrain, medulla similar to previous reports in mouse and rat¹, while CB expression is enriched in stratum moleculare cerebellum layer highlighting presence of Purkinje cells, and CR in the LC. **c, d** Tiled spectral images that were pseudo-colored to show distribution of calcium-binding protein PV, CB and CR (**c**) and TH and GAD65/67 (**d**). Enlargement of the boxed areas in **c** and **d** show that CB+ Purkinje neuron in CBL co-localized with PV, CR and VGAT, and TH+ dopaminergic neurons in SN and LC co-localized with GAD^{65/67}. Each brain region is composed of 4 tiled FOVs. Each FOV is a 500 μm^2 spectral image acquired at low-resolution scan resolving $\sim 1 \mu\text{m}^2/\text{pixel}$. Abbreviations: CA1, Cornu Ammonis 1; STR, Striatum; SN, Substantia Nigra; LC, Locus Coeruleus; CBL, Cerebellum; MO, Medulla Oblongata; CB, CALBINDIN; CR, CALRETININ; PV, PARVALBUMIN; TH, Tyrosine Hydroxylase; VGAT, Vesicular GABA Transporter; GAD^{65/67}, Glutamate Decarboxylase 65/67



By mapping the masks of these gated objects back onto the coordinates of the original segmented images (Fig. 3e), we created a cell phenotype map (CPM) that illustrated a more even distribution of hippocampal microglia relative to astrocytes (Fig. 3e, f1, Additional file 1: Fig. S3A). Astrocytes were enriched in hippocampal white matter and vascular regions (Fig. 3e, f2, Additional file 1: Fig. S3B) as they are integral parts of CNS white matter and blood–brain-barrier (BBB) architecture [42, 43]. Vascular CPM charts large and micro vessel boundaries (Fig. 3e, f3, Additional file 1: Fig. S3C). In the neuron CPM, masks are enriched in the granule cell layer of DG band, and are scattered throughout the image (Fig. 3e, f4, Additional file 1: Fig. S3D). These data highlight the utility of the combined segmentation approaches, enabling analyses analogous to those achieved in other tissue where spatial organization, expression, and molecular identities of single cells and proteopathy can now be determined and organized for human CNS.

Top-down spatial organization of cellular and proteopathy composition distinguishes hippocampal subregions and disease status

We combined our discretization strategies with prior knowledge of human hippocampal anatomy (i.e., top-down) to identify neuropathologic changes across stages of cognitive decline (defined by Thal phase, Braak stage, CERAD and ADNC scores, Additional file 1: Table S2B). Coronal hippocampal sections from three individuals were imaged, focusing on the DG to CA4 through CA1 subregions, and expanding outward (Fig. 4). Samples from cognitively normal (CN), cognitively impaired with no dementia (CIND), and ADD subjects were used to capture a wide spectrum of pathologic changes (Fig. 4a). Both MCI and CIND are attempts to define a state in-between normal cognitive function and dementia. Mild Cognitive Impairment (MCI) is a clinical diagnosis [44]. Cognitive Impairment with no Dementia (CIND) is

determined by neuropsychological test results [45, 46]. Single-plex spectral images of CN (Additional file 1: Fig. S4A–C), CIND (Additional file 1: Fig. S4D–F) and ADD (Additional file 1: Fig. S4G–I) hippocampus demonstrated larger, qualitative structures that can be captured by tiling numerous imaged fields together. For instance, VGLUT1 and VGLUT2 positivity demarking the CA and DG borders, respectively.

Given the known differences and progression of disease within AD hippocampal subregions [4], we first segregated all cells and protein aggregates into DG, CA4, CA3, CA2, and CA1 associations (Fig. 4b). We determined these boundaries for the subregions based on prior knowledge of morphological characteristics [47, 48] and expression of neuronal and pan-CNS markers including CALBINDIN, CALRETININ, MAP2, CD56, SYNAPTOPHYSIN (SYP), VGLUT1, and VGLUT2 (Fig. 4a, Additional file 1: Fig. S4) that have previously been shown to highlight boundaries [21, 24, 49]. Spectral images of CALBINDIN, CALRETININ, and MAP2, specifically showed anatomical delineation of CA4–CA2 (CALBINDIN), DG and Alveus (CALRETININ), joined by neuronal cytoarchitecture from CA4 to the subiculum (MAP2) (Fig. 4a, bottom panel). We then assigned cells and protein aggregates to their respective structures (Fig. 4b, Additional file 1: Table S5A). To assign cell identities, we applied a combination of FlowSOM [50] and manual meta-clustering strategies to parse out the objects into six distinct categories: neurons, microglia, endothelial cells, and non-immune glia which included both astrocytes and oligodendrocytes (Fig. 4b, lower panel). Astrocytes and oligodendrocytes were grouped together based on MBP, MAG, and GFAP expression, as their expression patterns overlapped enough at this lower resolution to make it difficult to assign individual labels for these subtypes.

Comparing the proportion of each cell type within the CA and DG subregions, we observed a higher proportion of protein aggregates in the CA1 subfield

(See figure on next page.)

Fig. 3 Spatial Organization and Molecular Identities of Cells and Proteopathy in ADD hippocampus is Revealed with Single-Cell and Object Segmentation. **a** Cartoons show examples of cells (astrocytes, microglia, vessels, neurons, and immune cells) and possible planar views in CNS tissue (dashed lines numbered 1 through 4). The representative photomicrograph (IHC-DAB) and MIBI-TOF (pseudo-colored spectral images) visually exemplify the corresponding focal planes (numbered 1 through 4) for the different cells, which are identified by their pan-markers (GFAP: astrocytes, Iba1-CD45: microglia, CD31-CD105-MCT1: vasculature, MAP2: neurons, CD45: immune cells). **b** Conceptual overview of nuclear and object segmentation approaches. With cellular segmentation, nuclear associated features (nuclei interiors, nuclei borders) are obtained using a pixel-based convolution neural network (DeepCell neural network) and custom pixel expansion around the nuclei, to generate cell segmentation masks for cell lineage assignments. Object segmentation was used to capture microglia and astrocytic processes, vascular boundaries, A β plaques, and PHF1-TAU NFTs and NTs. Masks for both discretized biological units are integrated to reveal their relationships in silico. **c** Photomicrograph (on the conductive gold slide, left panel) and corresponding MIBI-TOF spectral image (HH3 for nuclei, right panel) of human ADD hippocampus. White box highlights the re-rastered region that was used for analysis. **d** UMAP visualization of all segmented objects across all hippocampal FOVs, colored by lineage and proteopathy identities. Inset shows only A β plaques, and NFT-NTs overlaid on the UMAP. **e** Cell Phenotype Maps (CPM) of nuclear and object segmented masks labeled by their phenotype. **f** Composite CPM of all segmented masks with six inserts for a zoomed in view of cell identity overlaid onto segmentation masks for the hippocampal region. Regions 1–6 represent zoomed in images representative areas of CPMs in **e**

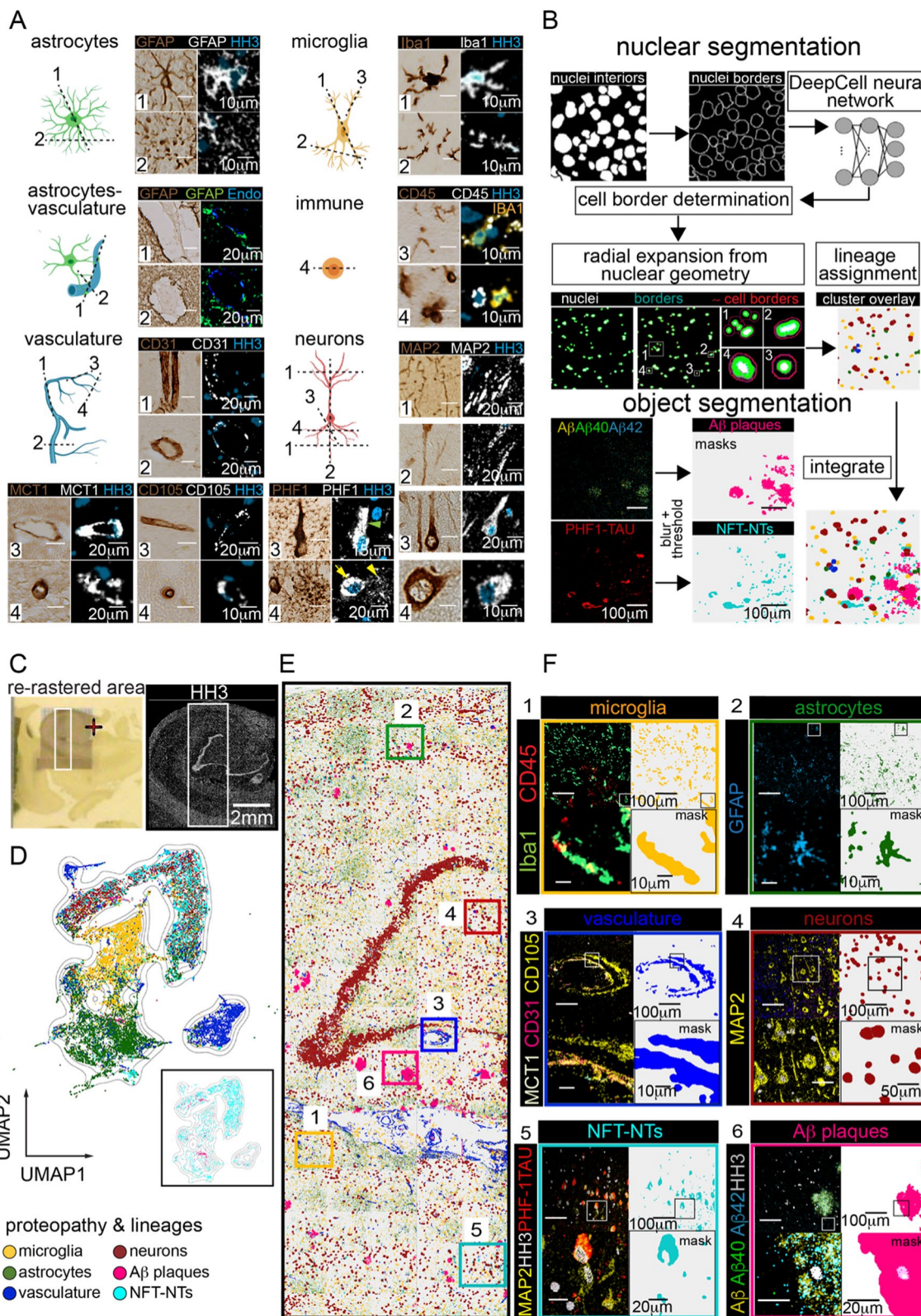


Fig. 3 (See legend on previous page.)

relative to other regions within the same sample, regardless of cognitive status (Fig. 4c, Additional file 1: Table S5B). In addition, the total number of protein aggregates increased in the tissue of cognitively impaired individuals (Additional file 1: Fig. S4J). We then considered whether proteopathies tended to lay in proximity to cell somas bound by our cellular segmentation. For each cell subtype, we counted the number of cells in direct proximity (i.e., overlapping pixels) to each proteopathy subtype and divided this value by the number of cells with no proteopathy overlap (Fig. 4d). Most cells did not exhibit direct proximity to A β plaque objects, particularly in the CN and CIND conditions. In the ADD individual, more cells lay in proximity to A β plaques, particularly for neurons in the CA1 and CA2 subfields, similar to previous reports [51]. For PHF1-TAU labeled NFT-NTs, a similar trend was found. In particular, microglia surrounding NFT-NTs doubled the number of microglia independent of NFT-NTs in the ADD CA1 subfield (Fig. 4d, *green circle*).

Building upon this observation, we contrasted those microglia that were NFT-NT associated (positive) or not (negative) (Fig. 4e). Microglia markers associated with reactivity [51], APOE, Iba1, CD33, and CD45, were consistently higher in NFT-NTs(+) relative to NFT-NTs(-) CA1 microglia, across all samples, with the highest expression in ADD (Fig. 4e). Microglia interacting with A β plaques did not show as strong of a difference in these reactive markers compared to microglia independent of A β plaques (Fig. 4f). Projecting an equal subset of microglia from all three samples onto a 2D-UMAP embedding, shows subsets of these reactive microglia associated with PHF1-TAU, particularly high Iba1(+) and APOE(+) in CA1 ADD

cells (Fig. 4g, *green circle*); and that while these cells exist across all individuals, they are most prominent in ADD (Fig. 4g, h, Additional file 1: Fig. S4K–L). This differential state of expression further reflects the possibility that immune cell reactivity may play a central role in AD severity, particularly an association with PHF1-TAU formation in CA1 subregion [51].

Bottom-up, data driven neighborhood analysis identifies common regions of neuropathology across individuals and severity

Given the level of neuropathological organization identified using previously defined hippocampal subregions, we investigated what other levels of spatial order could be revealed with a more data-driven approach to our multiplexed images. In addition to including the DG and CA regions, we also included cells from additional areas of the hippocampus captured including the alveus and subiculum. To this end, we employed a *bottom-up* workflow to isolate common signatures of hippocampal spatial identities, independent of previously known neuroanatomy or cognitive status. Using CytoMAP [18], we grouped local neighborhoods of similar protein aggregates and cell types across the three samples. After neighborhoods were calculated, a minimum number of common regions into which they could be grouped into was determined (*see Methods: Object co-proximity analysis*). Identified cells and protein aggregates were then assigned to these regions across each sample. A voronoi expansion from cell and object bearing areas was then used to cluster the surrounding neuropil (i.e., cell projections and extracellular matrix) into one of the regional groups (Fig. 5a). The final five regions determined across all samples were annotated as neuronal dominant (N), glial dominant (G), mixed proteopathy (M), A β plaque

(See figure on next page.)

Fig. 4 Cellular and proteopathy composition of hippocampal neuroanatomy. **a** Representation of the three imaged hippocampi to identify differences in AD pathological changes. Included are samples from people who were diagnosed as cognitively normal (CN), cognitively impaired, no dementia (CIND), or Alzheimer's Disease dementia (ADD). LFB and H&E histochemical staining of a serial section of each hippocampal slice imaged (Top). Pseudo-color overlay of CALRETININ (CR), CALBINDIN (CB), MAP2, and Histone H3 (HH3) acquired in each sample representing high-level neuronal morphology (Bottom). **b** Mask overlays of the cells and proteopathies collected by the segmentation methods described in Fig. 2, broken down by hippocampal neuroanatomy (Top) and cell or proteopathy subtype (Bottom). **c** Relative composition of each cell and proteopathy subtype within each anatomical subregion of each individual. **d** Ratio of proteopathy-associated cells to proteopathy-free cells in each anatomical region of each individual. Ratio of 1 indicates an equal number of proteopathy-associated cells to proteopathy-free cells, where PHF1-TAU NFT-NTs cell associations are shown in the top-panel and A β plaque cell associations in the bottom-panel. Callout indicates ADD, CA1 microglia with a high number of NFT-NTs associated microglia (*green circle*). **e** Normalized mean expression of microglia phenotyping channels in CA1 region of each individual, broken down by microglia with NFT-NTs association or those without. **f** Normalized mean expression of microglia phenotyping channels in CA1 region of each individual, broken down by microglia with A β plaque association or those without. **g** UMAP projections of CA1 microglia phenotyping channels in ADD. Gray represents CA1 microglia from CN, CIND samples (S4K–L for CN, CIND expression maps). Projection was calculated using Iba1, CD45, CD33, APOE, PHF1-TAU, A β 42, A β 40, and Pan A β markers. CIND and ADD are subsampled so that all conditions are represented by 447 microglia, the total number of CA1 microglia in the CN condition. **h** Image representation of tau-tangle and amyloid associated phenotypes described in E and F found in ADD CA1 microglia. Masks of microglia (yellow), tau NFT-NTs (cyan), and A β plaques (pink) (Left). Inset of microglia expressing phenotypic and proteopathy markers (Right). Abbreviations: CN, cognitively normal; CIND, cognitive impairment no dementia; ADD, AD dementia; DG, Dentate Gyrus CA1-4, Cornu Ammonis 1–4

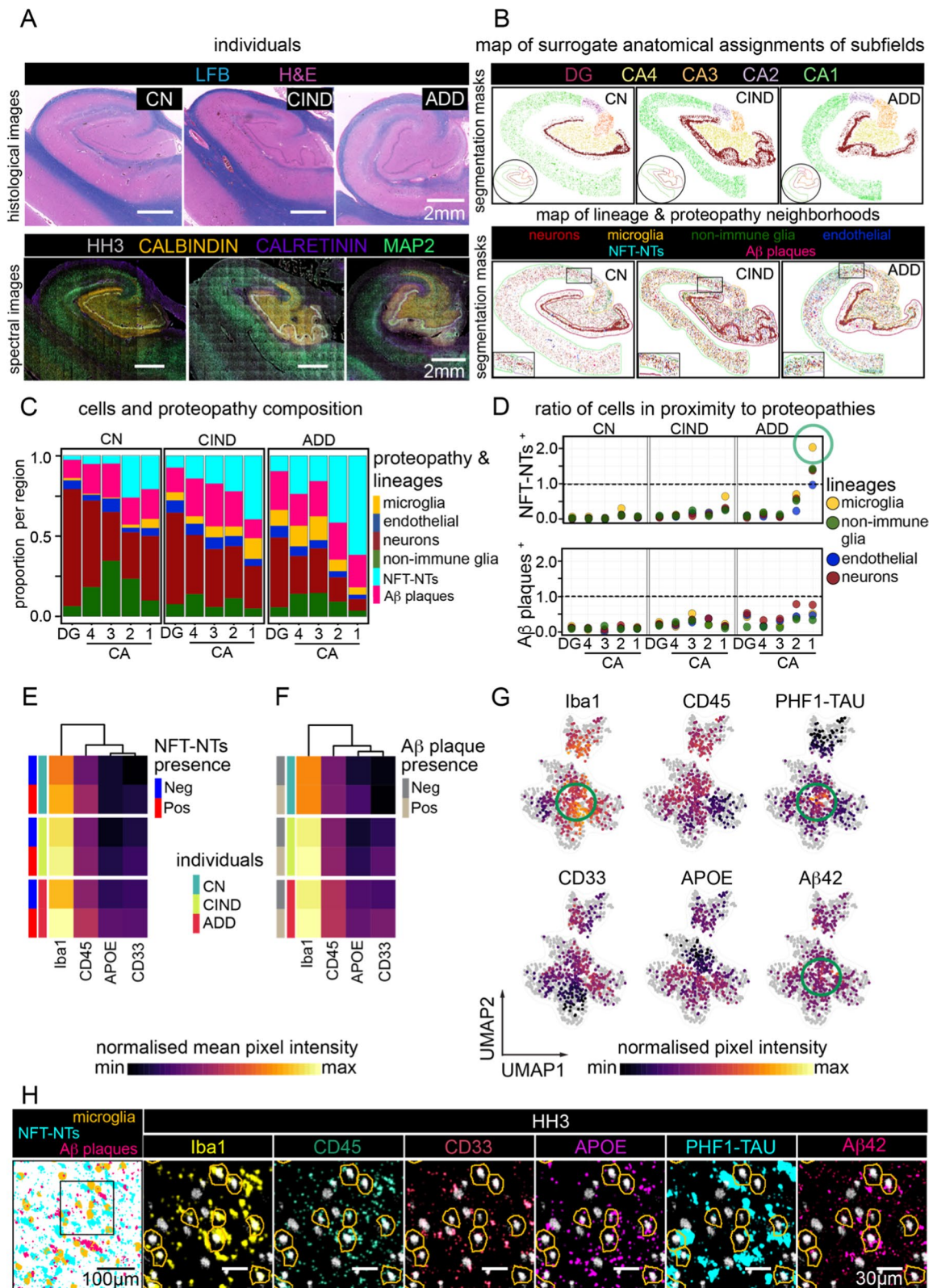


Fig. 4 (See legend on previous page.)

dominant (AP), or PHF1-TAU NFT-NTs dominant (TT) (Fig. 5b). The three proteopathy associated regions: M, AP, and TT were increased in representation with increasing cognitive impairment, while the relatively protein aggregate-free neuronal (N) and glial (G) cell regions decreased with increasing cognitive impairment, making up less than a quarter of the total ADD tissue (Fig. 5c, Additional file 1: Table 5SC). Unsurprisingly, even the cognitively normal hippocampus contained AP and TT regions (Fig. 5b, left purple and blue), consistent with the high prevalence of pre-clinical AD in older people. The mixed proteopathy M region represents a mixture of high proportions of neurons, A β plaques, and tau NFT-NTs (Fig. 5b, orange, Additional file 1: Table 5SC). Interestingly, this mixed region grew predominantly in the CA4-CA2 subregion, known for representing a resilient area of hippocampal degeneration [4]. CA1, a degeneration susceptible area, instead contained much more of the tangle dominant TT region as disease status worsened. Therefore, the M region could potentially indicate a transitional state of proteopathy development that could be related to resilience. Moreover, due to the data-driven nature of their identification we saw similar compositions of cells and proteopathy within a given region and across samples, regardless of cognitive diagnosis (Fig. 5d).

To integrate these regions and pathologic changes into a single model, we applied UMAP [37] dimensionality reduction to all cells and protein aggregates, comparing how they overlapped in disease severity or data-driven regions (Fig. 5e). While like cells or protein aggregates clustered tightly, there was some divergence with de novo region, suggesting unique combinations of protein expression with both anatomical location and spatially associated pathologic features. For example, a subset of neurons, non-immune glia, and microglia clustered with the TT region, separate from those in the N or G regions (Fig. 5e, *black circle*). Given the influence of de novo identified regions on cell and object embedding (Fig. 5e), we also quantified how cell-protein aggregate proximity itself

compared between the top-down anatomical (Fig. 4d) and data-driven regions (Fig. 5f). Regardless of sample staging, cells within the N- or G-regions showed very little proximity to pathologic objects, as expected. In the AP-region, nonimmune glia and neurons showed high proximity to neurons and nonimmune glia (Fig. 5f). The same trend held for PHF1-TAU NFT-NTs in proximity to cells in the TT-region. As pathologic changes increased, microglia once again stood out with the highest ratio of cells with NFT-NT proximity. These physical associations increased as severity worsened whether the nuclear associated cell body or protein aggregates were used as the basis for the proximity calculation (Additional file 1: Fig. S5A). In summary, while NFT-NTs development started in neuronal peripheries before accumulating in soma [38, 52, 53] our data suggests soma involvement continues as disease progresses.

With the connection between proteopathy formation and synaptic density, we further investigated the mean pixel expression of these markers across all identified data-driven regions in the hippocampus and how coincidence changed. Focusing on synaptic density, we calculated synaptic positive pixels by either excitatory (SYP(+), PSD95(+), and either VGLUT1(+) or VGLUT2(+)) or inhibitory (SYP(+), VGAT(+), GAD(+)) synaptic pixels. We then looked at the coincidence with PHF1-TAU and observed that while the highest percentage of PHF1-TAU formation in synapses occurred in ADD, all samples that contained the TT-region showed synaptic protein/PHF1-TAU localization (Fig. 5g), similar to what we have recently reported on synaptosomes [54]. Similar results were seen for A β plaque proximity to synaptic pixels in the AP region (Fig. 5g). This approach, as summarized in Fig. 5a, shows the ability to identify common pathological changes and neighborhoods across tissues representing a diversity of neuropathologic changes. Moreover, completely data-driven, bottom-up approaches, like the ones employed here, captured, and organized neuropathological features beyond the bounds of conventional

(See figure on next page.)

Fig. 5 Common de novo regions of cell and proteopathy composition are identified across different individuals. **a** Computational workflow used to isolate common regions of pathology (de novo regions) across CN, CIND, and ADD hippocampi independent of patient diagnosis. **b** De novo regions displayed across the entire tissue of each sample, CN, CIND, and ADD. N = Neuronal dominant region, G = glial (astrocyte/oligodendrocyte) dominant region, M = Mixed proteopathy region, AP = A β Plaque dominant region, TT = Tau NFT-NTs dominant region. **c** Relative composition of each de novo region across each individual hippocampus. **d** Relative composition of each cell and proteopathy subtype within each de novo region of each individual. **e** UMAP projection of all cells and proteopathies, calculated using much of the full panel (list in methods). De novo regions (left), cell and proteopathy classification (middle) and individual (right). Black ellipse denotes area of clustered cell lineages associated with TT region. **f** Ratio of proteopathy-associated cells to proteopathy-free cells in each de novo region of each individual. Ratio of 1 indicates an equal number of proteopathy cells to proteopathy-free cells. Tau tangle cell associations (Top) and A β plaque cell associations (Bottom). Top callout indicates high levels of tau tangle overlap in TT region; bottom callout indicates high A β plaque overlap in AP region. **g** Synaptic proteopathy presence. For each de novo region, all positive synaptic pixels with positive proteopathy signal (Top: tau, Bottom: amyloid) relative to all positive synaptic pixels. Excitatory synaptic channels (SYP(+), PSD95(+), and either VGLUT1(+) or VGLUT2(+)) and inhibitory synaptic channels (SYP(+), VGAT(+), GAD(+)) considered. Abbreviations: CN, cognitively normal; CIND, cognitive impairment no dementia; ADD, AD dementia; N, Neuronal dominant; G, Glial dominant; M, Mixed disease; AP, A β plaque dominant; TT, PHF1-TAU NFT-NTs dominant

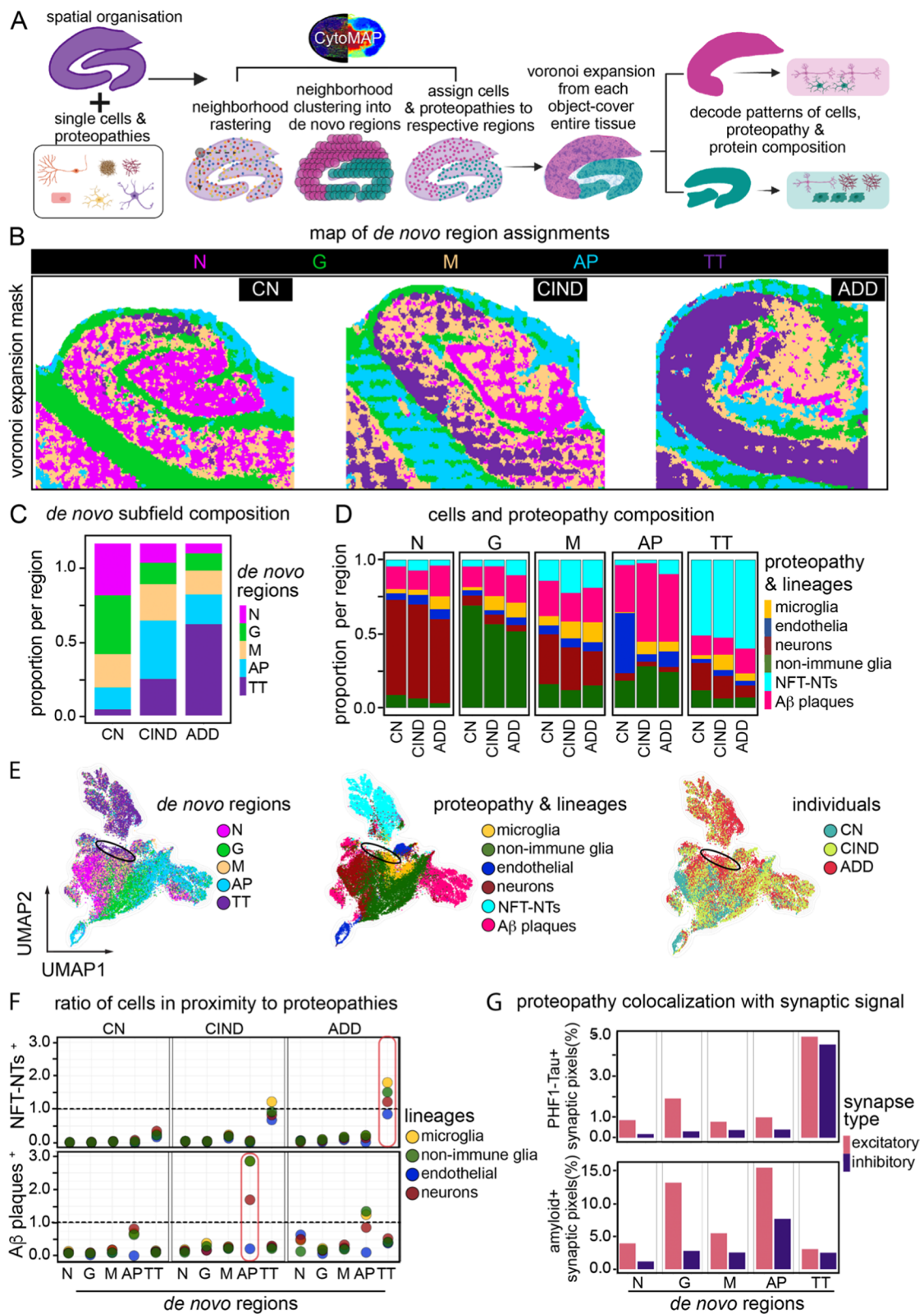


Fig. 5 (See legend on previous page.)

anatomical subregions potentially increasing the sensitivity to detect and classify dysfunction.

Clustering identifies mitochondrial MFN2 protein expression in persistent neurons associated with proteopathy-laden tissue regions

Leveraging the 14 proteins simultaneously measured to capture neuron identity and putative function in situ, we clustered these extracted cells using FlowSOM to identify 11 meta clusters. The expression distributions across these groups (Fig. 6a) and as seen by UMAP projection (Fig. 6b, c) and physical mapping (Additional file 1: Fig. S6A) showed that neurons fell broadly into two categories: (1) proteopathy associated (clusters 1, 2, 6, 8, 10), and cluster (2) non-proteopathy associated (clusters 3, 4, 7, 9, 11). While this analysis highlighted the previous trend of increased protein expression in proteopathy-associated cells (i.e., synaptic markers, Fig. 6a, Additional file 1: Fig. S5B) it revealed some functional neuronal subsets based on mitochondrial proteins and ubiquitination, e.g., MITOFUSION 2 (MFN2) (Fig. 6a, clusters 1, 2, 3, 4, 10) and POLYUBIQUITIN K48 (Fig. 6a, clusters 1, 2, 8).

As with the broader analysis of all objects (Fig. 5), neuron subclusters associated with proteopathy grouped together in a UMAP of neurons alone (Fig. 6c, left). As MFN2 was variably expressed across multiple non-proteopathy associated (clusters 3, 4) and proteopathy-associated neuronal clusters (clusters 1, 2, 10), we further investigated its expression and localization in the hippocampus. Interestingly, recent single nucleus analysis of transposon accessible chromatin (ATAC-seq) indicates that MFN2 is epigenetically restricted to neuron-specific lineages in human brain (Additional file 1: Fig. S6B) [55], re-enforcing its potentially unique role in neuronal function here. Neuronal MFN2 expression was positive primarily in non-proteopathy associated neurons, with a clear overlap in proteopathy associated neurons. (Fig. 6d, right, black arrow). These MFN2 positive neurons were more prevalent in proteopathy-associated regions

(MD, AP, TT) relative to the non-proteopathy associated regions (ND, GD) (Fig. 6d), suggesting that MFN2 expression may be associated with neuronal survival in the presence of stressors from proteopathy.

To understand MFN2-related persistence in proteopathy-laden regions, we compared the single-cell relationship between proteopathy expression and MFN2. Proteopathy-associated regions have higher proportions of MFN2(+) neurons relative to non-proteopathy associated regions in the CN hippocampus (Fig. 6f, Additional file 1: Table S6A). Additionally, in the ADD sample the percentage of MFN2(+) neurons in the non-proteopathy associated regions has jumped up considerably relative to the CN sample, further suggesting that this MFN2(+) expression may indicate an association with protection from the spread of proteopathy. Filtering by de novo region shows high abundance of MFN2(+), PHF1-TAU(+) neurons in the TT region (~20%) compared to the N region (~1%) (Fig. 6g, bottom, Fig. 6S6C; Additional file 1: Table S6B–C). These PHF1-TAU(+), MFN2(+) neurons can be seen throughout the TT region of the hippocampus, even appearing adjacent to PHF1-TAU single positive, as well as MFN2 single positive expressing neurons, regardless of disease status (Fig. 6h). Comparatively, the N region contained many more MFN2(+) single-positive neurons. This persistence of MFN2(+) neurons in areas of high tauopathy potentially reflects a neuronal protective response to injury as has been studied in animal and in vitro models of neuronal degradation [56]. MFN2's relationship with A β 42 did not show this same L-shaped distribution, especially in the AP region (Fig. 6g, top), suggesting that the presumed MFN2 response to injury may be specific to stressors that accompany pathologic Tau accumulation. We validated these expression patterns with IHC staining of PHF1-TAU, A β 42, MFN2 on each of the tissue samples (Additional file 1: Fig. S6D–F). Altogether, our study demonstrates both anatomical and data-driven approaches can be used to identify deep spatial

(See figure on next page.)

Fig. 6 Neuronal sub-clustering reveals relationship between MFN2 and persistent neurons in AD. **a** Heatmap showing mean normalized expression of neuronal markers after FlowSOM clustering. 11 clusters are broadly broken down into proteopathy and non-proteopathy associated phenotypes. Red arrow denotes MFN2 cluster expression. **b–d** UMAP projection of neurons alone, calculated based on same markers used to perform FlowSOM clusters in **a**. **b** Overlay of neuronal subclusters. **c** Overlay of clusters associated with proteopathy or no-proteopathy. **d** Overlay of normalized neuron expression of MFN2. **e** Proportion of neurons positive for MFN2 vs neurons negative for MFN2 for each de novo region. **f** Proportions of neurons positive for MFN2 across both de novo region and AD sample condition. **g** Expression profile of individual neurons for MFN2 and A β 42 in AP region (top) and MFN2 and PHF1-TAU in TT region (bottom). **h** Neurons in TT region of CA1, CN individual (top) and CA1, ADD individual (bottom). Black box represents areas of TT-associated tissue isolated for insets (left), zoomed in section of multiple neurons, colored by cluster ID's in A (middle), single or small groups of neurons representing persistent, TT cells (right). [1] MFN2(–), PHF1-TAU(–) neuron—Cluster 5. [2] MFN2(–), PHF1-TAU(+) neurons—Cluster 8. [3] MFN2(+), PHF1-TAU(–) neurons—Cluster 4. [4] MFN2(+), PHF1-TAU(+) neurons—Cluster 1. Abbreviations: CN, cognitively normal; ADD, AD dementia; N, Neuronal dominant; G, Glial dominant; M, Mixed disease; AP, A β plaque dominant; TT, PHF1-TAU NFT-NTs dominant

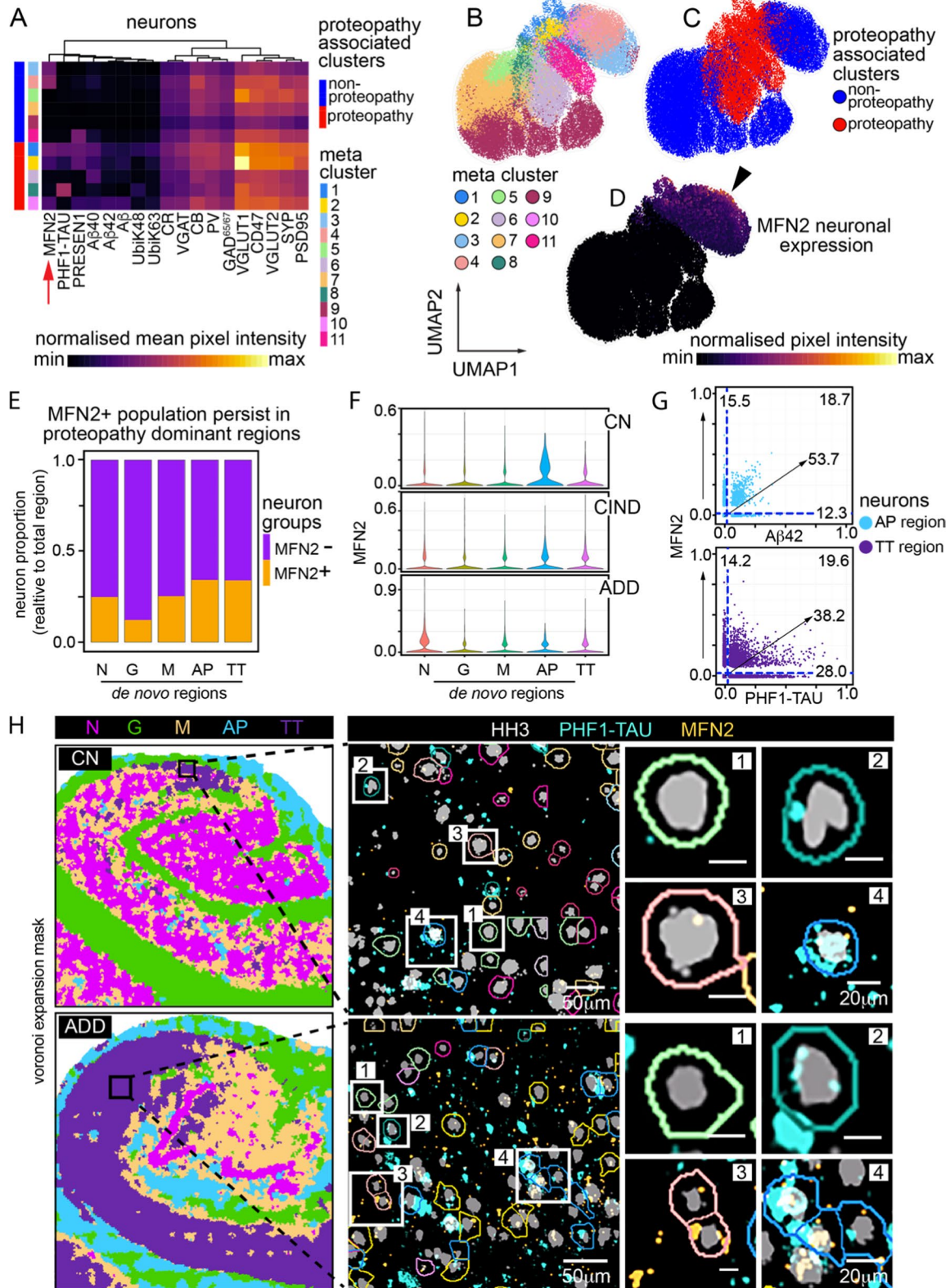


Fig. 6 (See legend on previous page.)

summaries of neuropathologic changes while identifying and subclassifying cells and features that compose them.

Discussion

In this study, we present an analytical framework leveraging MIBI-TOF spatial proteomic imaging as a resource for deep human neuropathology. We describe a workflow for the 36-plex image datasets generated from archival FFPE human brain tissues. We performed a broad IHC analysis that validated MIBI-TOF spectral images in multiple brain regions with neuropathologic changes spanning different stages of AD both clinically and pathologically. Our imaging panel was designed to phenotype brain cellular, structural, and proteopathy features while displaying well-known brain topologies. Segmentation of single-cell and disease features were phenotypically profiled, and their spatial organization in relation to local and global neighborhoods were explored. Finally, to delineate the cellular and molecular configuration in different clinic-pathological states of human AD, we showed the effectiveness of complementary approaches: a ‘top down’ method, that relied on classically stratified hippocampus subregions (DG through CA4-CA1), and a bottom-up data driven method that defined proteopathy-free and proteopathy-burdened cellular neighborhoods within the human hippocampus.

Notably, our study represents one of the most systematic, high-resolution analyses of *spatial* cellular and proteopathy composition in human brain. Age- (98.3 ± 1.5 yrs.), sex- (female), and *APOE* genotype- ($\epsilon 3/\epsilon 3$) matched samples were compared across carefully annotated clinico-pathologic samples from three research participants. We primarily focused on changes in the hippocampus, due to its implication early in AD pathogenesis [10]. We have configurations for the abundance of 34-plex proteins and their spatial distributions across 275,808 segmented cells, 25,130 Tau protein aggregates and 15,174 amyloid protein aggregates throughout the hippocampus and subiculum (54.6 ± 20.2 mm²).

We first used a ‘top-down’ approach to determine alignment with previous observations of hippocampal changes in AD [6]. We found that the hippocampus from the CN participant held A β plaques and PHF1-TAU NFT-NTs, albeit less than CIND and ADD hippocampus. Interestingly, proximity analysis showed that microglia interacted heavily with pathologic Tau, particularly in CA1 region. These microglia harbor increasing signatures of possible ‘disease-associated microglia’ (DAM) in ADD [1, 57]. We found similar associations using bottom-up data-driven approach for microglial and pathologic Tau. The discrepancy between A β plaque associated and NFT-NTs associated microglia reactive phenotypes in CA1 could be

indicative of an early vs late stage response, respectively. It is also possible more specific protein targets delineating NFT-NTs vs A β plaque-responsive microglia are needed to fully understand how microglia react to each proteopathy subtype. Our data also provides the ability to break down A β plaques into neuritic vs diffuse based on morphology metrics and PHF1TAU expression, though that was not explored here.

Our assessment of using the data-driven, bottom-up approach uncovered unique proteopathy and cellular spatial associations. The A β AP-region appeared more dominant in the CIND sample relative to the ADD sample, which is dominated by the pathologic Tau TT-region, perhaps a reflection of the established correlation of tauopathy with dementia in AD imaging [La Joie 2020]. The composition of N- and G-regions are particularly interesting as they represent regions of tissue that are mostly free from proteopathy and are found even in ADD. The exact relationship between proteopathy and glial lineages in the continuum of AD is unclear and could be regulated by several elements. For instance, immunogenicity towards A β or Tau oligomers in CN and CIND could vary from ADD samples [52, 58, 59], or ADD may have a more reactive microglial-dependent immune response relative to those present in the CN and CIND hippocampus [60].

The neuronal features that were imaged here are from those surviving neurons that have endured AD, including non-proteopathy bearing (PHF1-TAU and A β negative) and proteopathy-bearing neurons (PHF1-TAU or A β positive). We identified several molecular signatures that could have contributed to neuron survival. First, as in many animal models and recently in human tissue, we found pathologic Tau to be localized (but not exclusive) to neuronal synapses [54, 61]. *Drosophila* to mouse studies have shown that synaptic PHF1-TAU interferes with synaptic vesicles [41, 53, 62]. Second, we observed A β accumulation proximal to synaptic signal of glutaminergic and GABAergic neurons where others have suggested acute A β exposure can lead to GABAergic imbalance and altered neurotransmission [58, 63, 64].

Interestingly, we also observe potential compensatory mechanisms, including ubiquitin proteasome system (UPS) and mitochondrial bioenergetics (i.e., MFN2, Fig. 6) across all individuals, but most prominently in the person with ADD. Here, we detected K48-linked ubiquitin in proteopathy rich neurons, in particular preferential enrichment in NFT-NTs. Similar enrichment of K48-linked ubiquitin has been reported in older AD brains [65]. The role of preferential K48-ubiquitination on PHF1-TAU oligomers is still unclear; however, others have proposed a “soak-up” mechanism to sequester the toxic effect of protein aggregates and promote

UPS mediated clearance [66, 67]. Importantly, we also found a prevalence of MFN2 expression in proteopathy-burdened hippocampal regions, particularly in areas of pathologic Tau. Here MFN2, an outer membrane mitochondria fusion protein, could maximize the oxidative capacity of the disease-free neurons, a potential response to a stressor associated with accumulation of pathologic Tau. MFN2 also inhibits mitochondrial fission, preventing autophagy, and thus helping to maintain mitochondria for the surviving neurons [68–70]. Given the role of neuron-mitochondrial dysfunction found in multiple models of AD, MFN2 may represent an important target for maintaining survival in proteopathy-susceptible neuron populations. Taken together, our bottom-up data-driven approach of studying disease neighborhoods mapped out phenotypic changes as a function of proteopathy and identified potential coping mechanisms of hippocampal pyramidal neurons to withstand the stressors of proteopathy-associated AD pathogenesis. Although we focus on neuronal cell neighborhoods here, the unsupervised approach can be extended to map the response of proteostatic stress on glial and vascular cells. Targeted approaches for the other key homeostatic populations (microglia, astrocytes, and oligodendrocytes) are imperative in understanding the effect of cellular crosstalk (feedback and feedforward), heterogeneity in activity, population abundance, and localization to disease and cognitive status. The framework we have created here could be applied to investigate CNS cellular biology in all these scenarios.

Like many neurodegenerative diseases, AD is phasic, undergoing biochemical changes that induce cellular stress and remodeling of anatomical neighborhoods. Detailed mapping of the biochemical, cellular, and architectural changes can help develop strategies for dynamic models of disease, potentially from a limited number of patient samples. Future studies on larger patient cohorts could order individuals, based on the spatial features we have derived here, along disease pseudo-time as means to quantify disease progression as reflected in spatio-molecular changes. Pseudo-time ordering has been used for fate mapping, tumor progression, hematopoietic development, and to map the layered and cell-specific degeneration of hippocampal sclerosis [71–77]. Inferred disease staging can help sort the temporal function of biochemical and molecular regulators in AD clinical progress, identify founding factors in AD, and uncover disguising factors that potentially play roles for neurological resilience in ‘healthy’ individuals. Such modelling of multiplex imaged human brain tissue may help understand whether A β 42 oligomers followed by PHF1-TAU oligomers are primers or followers to degeneration, or if other

underlying bad molecular actors precedes proteopathy (e.g., aberrant immune activation).

MIBI-TOF and our study also had limitations. First, because MIBI-TOF imaging scans physically sputter material off the imaged sample, it is thus destructive. Still, thin sections can be re-scanned multiple times and serial sections can be used for further experimentation. Second, this is a probe-based technology that largely relies on antibody availability and specificity for detection of limited target antigens (~40), though the staining and integration of serial sections with different antibody panels can exponentially increase the N-dimensionality of probing factors. Still, probe-based technologies also tend to be more robust and quantitative compared to de novo techniques that offer a wider, albeit variable, array of multiplexing. Although unexplored here, as an elemental mass spectrometry method, MIBI-TOF can simultaneously quantify presence of essential and non-essential metals, such as Fe, Cu, Mn, Zn, and Al, along with the N-number proteins which can contribute to AD pathogenesis [78]. Third, findings are contingent upon the rigor of patient and postmortem tissue characterization (i.e., clinical diagnosis and neuropathological assessment), and tissue integrity. Dynamic measurement of postmortem human brain tissue is not trivial, requiring a large number of carefully annotated samples from people of varying ages. Nevertheless, inferences of AD progression can be made with limited postmortem sample via use of systematic characterized subjects, tissue, multiplex approaches, and data-driven modelling. Compatibility, as we have shown here, with the archival (i.e., FFPE) format these tissues are typically stored in is critical for successful interrogation.

The major advantage of MIBI is a combination of relatively fast whole tissue imaging while maintaining cellular resolution and multiplexed feature capture with relatively low cost per sample [15–17, 20]. Bright-field imaging (e.g. IHC) does not have the ability to identify more than a handful markers at once (usually no more than 2–3). Fluorescent multiplexing offers similar resolution and target numbers [79], but takes much more time to image the same number of samples or tissue as cyclic washes are usually involved, and image integration can take a long time [17]. However, both of these options are cheaper than MIBI. Compared to the Nanostring GeoMX system and others like it [80, 81], while they can capture higher number of targets for purposes of discovery, their throughput, cost, and limited sampling present challenges for large tissues across high numbers of patients. To capture the local micro-environments fully across brain regions, both cellular resolution, neuropil, and larger structures like vasculature are needed to accurately

define neighborhoods. MIBI enables all of these structures captured simultaneously while Nanostring is limited to selected cells or ROI's around said cells, creating a tradeoff of cellular resolution and tissue resolution MIBI does not need to make. Thus, new cellular level features methods like ours discovers will be ripe for follow-up analysis with orthogonal -omic technologies like these. While at the same time, our spatial proteomic approach with MIBI could help better contextualize new regulatory targets in larger tissues and cohorts with (sub)cellular resolution.

Our work paves the way for the development of novel approaches for quantitative, simultaneous, multiplexed imaging in human neuropathology. Utilizing the wealth of RNA sequencing data [82, 83], and together with an integrated RNA and proteomic approaches [84] disease mechanisms driving cell–cell and cell–proteopathy interactions can be isolated and now imaged at the proteomic level in their native tissue with our multiple, high-resolution MIBI-TOF platform. Combining multiple spatial biomolecular technologies (e.g., MALDI, RNA-ISH, super-resolution microscopy) will enable even deeper understanding of biomolecular interplay in neurodegeneration. Integration of this spatially multiplexed data with further clinical histories will drive insights on possible cellular mechanisms underlying symptomatic disease progression or resilience in CNS disease.

Materials and methods

Contact for reagents and resource sharing

Further information and request for reagents and resources (Additional file 1: Table S7) should be directed to and will be fulfilled by the Lead Contact, Sean Curtis Bendall (bendall@stanford.edu).

Experimental model and subject details

Human sample acquisition and patient consent

Human brain samples were obtained from Stanford Pathology Department. Average post-mortem interval of tissues ranges between 2.9 and 15 h. Clinical diagnosis and neuropathological scores were generated by Stanford clinicians and pathologist. The clinical diagnosis was based on DSM-IV criteria. AD neuropathologic change and severity scores were evaluated by NIA-AA guidelines [5, 85]. All three cases (CN, CIND and ADD) also were evaluated for neuropathologic evidence of vascular brain injury, Lewy body disease, or hippocampal sclerosis by NIA-AA guidelines and those with any evidence of these three neuropathologic changes were excluded. Neuropsychological test battery results for CN participants within 1 year of death were in the upper three quartiles for the

research cohort. As a note for readers, MCI reflects a medical diagnosis, whereas CIND reflects a prodromal state defined by neuropsychological tests only and is what the primary samples were based on [44–46]. Full details of Thal, Braak, ADNC, and CERAD scoring are included in Additional file 1: Table S2B.

MIBI-TOF experimental details

Antibody conjugation

Primary antibodies, reporter isotopes, and titers can be found in Additional file 1: Table S1. Metal conjugation of primary antibodies were prepared as described previously [86] and is detail in <https://doi.org/10.17504/protocols.io.bhyej7te> [87]. Post conjugation antibodies were diluted in Candor PBS Antibody Stabilization solution (Candor Bioscience GmbH, Wangen, Germany) to 0.1 mg/ml, and stored at 4 °C for short-term use and for long-term used were lyophilized using the following protocol <https://doi.org/10.17504/protocols.io.bhmgj43w> [88].

MIBI staining

FFPE tissue blocks of whole hippocampus or brain TMA were sectioned using a microtome. The 5 µm thick tissue sections were mounted onto silanized-gold slides for MIBI-TOF staining. Gold slides containing tissue were baked at 70 °C overnight. Tissue sections were then processed and stained with a cocktail of antibodies as is detailed in https://doi.org/10.17504/protocols.io.byzrp_x56 [89]. Stained tissue slides were preserved under vacuum until required for MIBI-TOF scan.

IHC staining

For IHC validation of primary antibody target specificity, FFPE human hippocampus or brain TMA, of 5 µm thickness, were sectioned onto standard glass slide. Slides containing tissue were baked at 70 °C overnight. Tissue sections were then processed and stained using the Sequenza method with single post-metal conjugated primary antibody. Staining method is detailed in <https://doi.org/10.17504/protocols.io.bf6ajrae> [90].

MIBI-TOF image acquisition

Spectral images of stained hippocampus or brain TMA tissue were obtained using the MIBI-TOF mass spectrometer equipped with a Hyperion ion source. Xenon primary ions were used to sputter the stained tissue sample at doses ranging from average 17.9 nAmp ms pixel²/µm² for 500 µm² to 52.3 nAmp ms pixel²/µm² for 400 µm² FOVs. MIBI-TOF parameters used in acquiring all imaging data is detailed in Additional file 1: Table S3.

TOF calibration and spectral image generation

Post-acquisition, time of flight was calibrated using sodium (Na^+ 22.99 amu) and gold (Au^+ 196.97 amu). Counts for each mass were determined by the start and end of their respective spectral peaks. For instance, in CD56 antibody conjugate to Nd145, the counts for masses between 144.7 and 145.2 were used and so on. Spectral images for each FOV were generated by converting the mass-spec pixel data to multidimensional tiffs.

Image processing (background subtraction and denoising)

After extracting raw data, images were background removed, noise corrected, and tiled to form a composite image of the entire issue section. Background (Bg) signal and noise were removed using a streamline in house developed graphic user interface (gui) in Matlab (<https://github.com/angelolab/MAUI>). Bg signal highly correlate with Au channel from the slide, on the edges and holes in the tissue. The Bg signal ($T=0.1-0.2$, gaussian kernel with $R=1$ pixel) were removed from all channels. High frequency signal was considered noise from MIBI-TOF brain spectral data. Also, many signals from brain tissue, especially those from synaptic markers (SYN, PSD95, VGLUT1/2, VGAT), CD56, and CD47 are dense signals. These dense signals were used as the high frequency cut-offs for our Fast Fourier transform (FFT) approach to filter noise from all brain spectral images. Furthermore, signal spill over due to adducts and oxides, were compensated for the following conjugates: pASyn to A β , Iba1 to PSD95, GFAP to CD105, MBP to MCT1, MCT1 to CD33, TAU to MFN2, TH, MAP2, pTDP43, 8OHG and A β .

Processed data were stored as image Tiff files and .mat files for data processing and analysis.

Image stitching and normalization for visualization

Image stitching for visualization purposes was performed using custom python scripts within the Fiji/ImageJ image processing environment and utilizing existing plugins. Individual tiles first underwent a flat-field correction (FCC) within tissue masked areas. Specifically, tissue masks were generated using the thresholded C12 channel, as well as the inverse of thresholded Au197 and Empty139 channels. The FCC reduces the effects of mass dependent aberrations within the fields of view. The FCC is performed by summing, down sampling, and smoothing each channel from each field of view. This smoothly varying intensity map was then used to normalize each individual field of view channel. Additionally, to correct for spatially uneven detection, each tile was cropped by 1% on each side to eliminate edge effects, followed by

an additional FCC. This second FCC generates an intensity map for each tile by averaging, down sampling, and smoothing all channels, the result of which should average out biologically distinct distributions, leaving only an intensity response map. These maps are then respectively used to normalize each field of view's channels. The "Grid stitching" plugin then stitched these tiles together, with overlaps specified by the acquisition parameters. Each channel was then smoothed using a 2-pixel median filter, and linearly auto scaled to maximize the visual contrast for each channel. For visualization with MIBItracker, each image was down sampled to have the largest dimension equal to 2048 pixels. For many channels it was possible to reduce the gridded pattern artifact via bandpass filtering in Fourier space. This is acceptable as biological information is typically not aligned in this way. However, channels whose signal varied significantly over a low frequency across the imaged area were not bandpass filtered, as these components would also be removed. Related to this work, tiling functionalities are now available through the Ionpath's github repository <https://github.com/ionpath/mibilib>.

Additional stitching was done via a custom Matlab tiling script linking start and end coordinates of each scanned images.

Data processing and discretization analysis

Global expression pattern

Background removed and denoised image TIFs (one file per marker) containing the pixel intensities were used to determine the global expression levels per TIF file. Each pixel represents marker expression intensity in a 500 or 400 μm^2 area and where the variances of marker expression between different areas of the human brain.

Cellular segmentation

Nuclei segmentation was carried out using an adapted version of DeepCell [10, 34, 36]. *Training data.* Epithelial cell nuclei stained with dsDNA or HH3 were used as core training data as described previously [10]. *Segmentation of brain images.* All images (841 TIFs of HH3) were subjected to the trained network and were normalized in the same fashion as the training images, by subtracting an averaging filter and dividing by the std of the whole image. *Post processing.* Probability map for the 'nuclear interior' were thresholded and separated to generate nuclear masks as described before [10]. Cell border expansion on these nuclear masks were performed to partially capture cell bodies. Nuclear morphology information including, area, circularity, eccentricity, major and minor axis lengths (*regionprops*, MATLAB 2019b) were used to infer cell type between neuronal and glial

cells due to their large differences in cell versus nucleus sizes. To calculate mean marker expression values for each segmented cell, the TIFs containing the pixel expression values were combined with the expanded nuclear segmentation masks. A data frame containing information of each segmented cell, with an allocated cellular ID (row), is populated with the corresponding values of each marker expression (column). In addition, supporting overlay files that track the spatial information for each cell in each FOV were created. To linearize the data and deal with extreme outliers, all mass channels were log-transformed in addition to 99th quantile normalization in RStudio (Version 2.1).

Object segmentation

Thus far, we have used nuclear segmentation and blanket marker expression data in our analysis. To enable the use of object structures, such as A β plaques and NFT-NTs, we had to employ EZSegmenter—a MATLAB *region-props* thresholding-based segmentation GUI developed in-house and available as a part of the MIBI image processing toolkit here: <https://github.com/angelolab/MAUI>. Multiplexed TIF images from multiple FOVs are loaded into the GUI. Channel select displays signal intensities of MIBI images and are used to determine object masks. Additional settings (e.g. Gaussian Blur, minimum and maximum object pixel size) are fixed across FOVs. Masks are then used to extract pixel—level signal intensities across each channel and then cell size normalized before import into an output cell table csv file. In addition to segmenting A β plaques, NFT-NTs, and vessels, we were able to improve cell segmentation by including parts of cells that had their nuclei mechanically destroyed by the tissue preparation process or were not scanned by the MIBI. All parameters for each objects segmented can be found in Additional file 1: Table S3B. This new data underwent similar normalization steps as the original segmented cell data.

Manual gating ADD hippocampus (1024 \times 1024 images)

Akin to classical single cell analysis in cytometry, step-wise manual gating strategy starting from the lowest to highest mean pixel levels was carried out. We first gated on CD31+, CD105+ and MCT1+ to label the endothelial fraction, the remaining fraction were gated for Iba1+ and CD45+ to classify microglia, and subsequently GFAP+ was used to label the astrocytes. The final remaining meta fraction was labeled as neurons and oligodendrocytes. Gated populations were overlaid back onto the spectral images and incorrect labels were curated using a multi-channel imaging platform (Mantis viewer, Parker Institute, <https://mantis.parkerici.org/>).

Single object clustering and phenotyping

512 \times 512 CN, CID, and ADD images

Initial gating was performed using common marker panels. Endothelial CD31, MCT1, CD105: endothelial cells; CD45 and Iba1: microglia; GFAP: astrocytes.

1024 \times 1024 ADD images

To assign a lineage for each segmented cell, a sequential gating strategy was performed on the transformed marker expression, starting with CD31, MCT1, CD105 for endothelial cells; then CD45 and Iba1 for microglia; then GFAP for astrocytes. Remaining ungated cells were then assigned as neurons. The accuracy of manual gating was curated by a multichannel imaging application MantisViewer. The curated expression data was imported back into R for UMAP analysis, heatmaps and object co-proximity analysis. Masks of neurons identified by cellular segmentation were merged with masks of the object segmented data (microglia, astrocytes, endothelia, A β plaques, and tau NFT-NTs) to obtain a comprehensive repertoire of neuronal and non-neuronal cell types, and proteopathy features.

Object co-proximity analysis

Thresholds for the co-proximity analysis were empirically determined by calculating the shortest physical distance of the periphery of a cell to another cell or proteopathy feature in a pairwise manner, and in a predefined pixel-radius. A distance interaction matrix was calculated for each pixel-radius, for 25(\approx 10 μ m), 50(\approx 20 μ m), 100(\approx 39 μ m), 150(\approx 59 μ m), 200(\approx 78 μ m), 250(\approx 98 μ m) and 300(\approx 117 μ m) pixel-radius, and the optimal distance used for thresholding was based on counts and frequencies of object pairwise interaction. The threshold of $t=25$ -pixel-radius for NVU, $t=50$ -pixel radius for NFT-NTs and $t=100$ -pixel radius for A β plaques. The null hypothesis (H₀): all objects do not interact with each other and are equidistantly dispersed throughout each FOV. The baseline object interaction (H₀) frequencies were calculated via the number of objects that would appear within threshold radius (t) by chance. The random chance was estimated by taking a proportion of objects appearing within the area of the thresholded radius and the entire FOV. Since this analysis was performed on individual FOVs, the ratio of the observed neighbor counts versus their estimated counterparts were used to normalize the values between FOVs.

Software, data and code availability

Software for running the MIBI-TOF equipment was developed by SAI (MiniSIMS 2 Data Systems Version

5.5.4.0). All the data described in this work, including channel images, segmentation masks and cellular and object identities can be accessed through a web interface and downloaded at <https://mibi-share.ionpath.com>. The code for the analysis can be downloaded at https://github.com/bryjcannon/MIBI_Brain_Analysis. All the information required for cell segmentation including the manual training data, trained neural networks, and code for training and running DeepCell (now incorporated into a cell segmentation known as MESMER) are available at Ark-Analysis <https://github.com/angelolab/ark-analysis>.

Supplementary Information

The online version contains supplementary material available at <https://doi.org/10.1186/s40478-022-01465-x>.

Additional file 1: Supplementary Figures and legends S1 through S6.

Acknowledgements

We would like to thank Dr. Rosario Sanchez-Pernaute for her critical inputs on the manuscript. Humphrey Vijayaragavan-Bossé and Teddy Cannon-Merchant for their unconditional love and moral support. Dr. Edward Fox for his assistance with the brain tissue repository. We would also like to thank Bangelo Broomwagon team of scientists (Mako Goldston, Christine Camacho, Ferda Filiz and Angie Dawn Spence) for their wet lab support.

Author contributions

KV, BJC, and SCB conceptualized, designed, and executed the project. KV, MB, JPO, DMr, DMA, ZK, TB, AR, validated antibodies and protocols on IHC and MIBI for human brain tissue. KV and MB acquired all the MIBI images. RMA and MB maintained and troubleshot MIBI instrument. AB designed MIBI TIFF processing tools for noise and background removal. KV and DT analyzed single FOVs and sample hippocampus for pixel level and cell / object level differences. BJC designed the segmentation tools for non-standard cell and proteopathy objects, as well as analysis of larger hippocampal datasets across anatomy and disease status. NG provided DeepCell segmentation of standard cell types. EFM provided additional analysis of cell neighborhoods. SB, TM provided the human brain tissue for study. KM, TM, SCB provided review and editorial assistance of the manuscript. MRC provided the ATACSeq data and analysis. KV and BJC were the primary writers of the manuscript. All authors read and approved the final manuscript.

Funding

This work was supported by NIH grants R01 AG056287, R01 AG057915, R01 AG068279, U19 AG065156, UH3 CA246633 and P30 AG066515. N.F.G. was supported by NCI CA246880-01 and the Stanford Graduate Fellowship. Canadian Institute of Health Research Postdoctoral Fellowship (J.P.O.) T32 AI007290 to B.J.C and E.F.M. D.M. was supported by Schweizerischer Nationalfonds zur Förderung der Wissenschaftlichen Forschung (P2ZHP3_181563), Novartis Foundation for medical-biological Research (#18B067), and the Glenn Foundation for Medical Research Postdoctoral Fellowship in Aging Research.

Availability of data and materials

The datasets generated during and/or analyzed during the current study are available in the Stanford Data Repository at <https://doi.org/10.25740/tx581jb1992>.

Declarations

Ethics approval and consent to participate

All human tissue used in our study will be de-identified archival material. No tissue will be acquired prospectively for this study. Consequently, these studies did not constitute human subjects research.

Consent for publication

Not applicable.

Competing interests

MA and SCB are consultants for and shareholders in Ionpath Inc. that commercializes MIBI technology. MA and SCB are inventors on and receive royalties for patents relating to MIBI technology licensed to Ionpath Inc. YS was an employee of Ionpath Inc. at the time analysis was done on this manuscript. All other authors declare no competing interests.

Author details

¹Department of Pathology, School of Medicine, Stanford University, Stanford, CA, USA. ²Ionpath, Inc, Menlo Park, CA, USA. ³The Gladstone Institutes, San Francisco, CA, USA.

Received: 2 September 2022 Accepted: 18 October 2022

Published online: 04 November 2022

References

- Keren-Shaul H, Spinrad A, Weiner A, Matcovitch-Natan O, Dvir-Szternfeld R, Ulland TK et al (2017) A unique microglia type associated with restricting development of Alzheimer's disease. *Cell* 169:1276–1290.e17
- Mrdjen D, Pavlovic A, Hartmann FJ, Schreiner B, Utz SG, Leung BP et al (2018) High-dimensional single-cell mapping of central nervous system immune cells reveals distinct myeloid subsets in health, aging, and disease. *Immunity* 48:599
- Acioglu C, Li L, Elkabes S (2021) Contribution of astrocytes to neuropathology of neurodegenerative diseases. *Brain Res* 1758:147291
- Braak H, Braak E (1991) Neuropathological staging of Alzheimer-related changes. *Acta Neuropathol* 82:239–259
- Hyman BT, Phelps CH, Beach TG, Bigio EH, Cairns NJ, Carrillo MC et al (2012) National Institute on Aging–Alzheimer's Association guidelines for the neuropathologic assessment of Alzheimer's disease. *Alzheimer's Dementia* 8:1–13
- Mrdjen D, Fox EJ, Bukhari SA, Montine KS, Bendall SC, Montine TJ (2019) The basis of cellular and regional vulnerability in Alzheimer's disease. *Acta Neuropathol* 138:729–749
- Thul PJ, Åkesson L, Wiking M, Mahdessian D, Geladaki A, Blal HA et al (2017) A subcellular map of the human proteome. *Science* 356:eaal3321
- Gilissen EP, Staneva-Dobrovski L (2013) Distinct types of lipofuscin pigment in the hippocampus and cerebellum of aged cheirogaleid primates. *Anat Rec* 296:1895–1906
- Guardo GD (2015) Lipofuscin, lipofuscin-like pigments and autofluorescence. *Eur J Histochem EJH* 59:2485
- Keren L, Bosse M, Marquez D, Angoshtari R, Jain S, Varma S et al (2018) A structured tumor-immune microenvironment in triple negative breast cancer revealed by multiplexed ion beam imaging. *Cell* 174:1373–1387.e19
- Dora L, Agrawal S, Panda R, Abraham A (2017) State-of-the-Art methods for brain tissue segmentation: a review. *IEEE Rev Biomed Eng* 10:235–249
- Greenbaum S, Averbukh I, Soon E, Rizzuto G, Baranski A, Greenwald N et al (2021) Spatio-temporal coordination at the maternal-fetal interface promotes trophoblast invasion and vascular remodeling in the first half of human pregnancy. *Biorxiv* 28:406
- McCaffrey EF, Donato M, Keren L, Chen Z, Delmastro A, Fitzpatrick MB et al (2022) The immunoregulatory landscape of human tuberculosis granulomas. *Nat Immunol* 23:318–329
- Risom T, Glass DR, Averbukh I, Liu CC, Baranski A, Kagel A et al (2022) Transition to invasive breast cancer is associated with progressive changes in the structure and composition of tumor stroma. *Cell* 185:299–310.e18
- Liu CC, McCaffrey EF, Greenwald NF, Soon E, Risom T, Vijayaragavan K et al (2021) Multiplexed ion beam imaging: insights into pathobiology. *Annu Rev Pathol Mech Dis* 17:1–21
- Liu CC, Bosse M, Kong A, Kagel A, Kinders R, Hewitt SM et al (2022) Reproducible, high-dimensional imaging in archival human tissue by multiplexed ion beam imaging by time-of-flight (MIBI-TOF). *Lab Invest* 102:762–770
- Hickey JW, Neumann EK, Radtke AJ, Camarillo JM, Beuschel RT, Albanese A, et al (2021) Spatial mapping of protein composition and tissue

- organization: a primer for multiplexed antibody-based imaging. *Nat Methods* 1–12
18. Stoltzfus CR, Filippek J, Gern BH, Olin BE, Leal JM, Wu Y et al (2020) CytoMAP: a spatial analysis toolbox reveals features of myeloid cell organization in lymphoid tissues. *Cell Rep* 31:107523–107622
 19. Schnell SA, Staines WA, Wessendorf MW (1999) Reduction of lipofuscin-like autofluorescence in fluorescently labeled tissue. *J Histochem Cytochem* 47:719–730
 20. Keren L, Bosse M, Thompson S, Risom T, Vijayaragavan K, McCaffrey E et al (2019) MIBI-TOF: a multiplexed imaging platform relates cellular phenotypes and tissue structure. *Sci Adv* 5:eaa5851
 21. Herzog E, Takamori S, Jahn R, Brose N, Wojcik SM (2006) Synaptic and vesicular co-localization of the glutamate transporters VGLUT1 and VGLUT2 in the mouse hippocampus. *J Neurochem* 99:1011–1018
 22. Liguz-Leczna M, Skangiel-Kramska J (2007) Vesicular glutamate transporters (VGLUTs): the three musketeers of glutamatergic system. *Acta Neurobiol Exp* 67:207–218
 23. Vigneault É, Poirel O, Riad M, Prud'homme J, Dumas S, Turecki G et al (2015) Distribution of vesicular glutamate transporters in the human brain. *Front Neuroanat* 9:23
 24. Rivera P, Arrabal S, Cifuentes M, Grondona JM, Pérez-Martín M, Rubio L et al (2014) Localization of the cannabinoid CB1 receptor and the 2-AG synthesizing (DAGLa) and degrading (MAGL, FAAH) enzymes in cells expressing the Ca2+-binding proteins calbindin, calretinin, and parvalbumin in the adult rat hippocampus. *Front Neuroanat* 8:56
 25. Hawrylycz MJ, Lein ES, Guillozet-Bongaarts AL, Shen EH, Ng L, Miller JA et al (2012) An anatomically comprehensive atlas of the adult human brain transcriptome. *Nature* 489:391–399
 26. Hof PR, Glezer II, Condé F, Flagg RA, Rubin MB, Nimchinsky EA et al (1999) Cellular distribution of the calcium-binding proteins parvalbumin, calbindin, and calretinin in the neocortex of mammals: phylogenetic and developmental patterns. *J Chem Neuroanat* 16:77–116
 27. Bjerke IE, Yates SC, Laja A, Witter MP, Puchades MA, Bjaalie JG et al (2021) Densities and numbers of calbindin and parvalbumin positive neurons across the rat and mouse brain. *Iscience* 24:101906
 28. Fortin M, Marchand R, Parent A (1998) Calcium-binding proteins in primate cerebellum. *Neurosci Res* 30:155–168
 29. Bastianelli E (2003) Distribution of calcium-binding proteins in the cerebellum. *Cerebellum* 2:242–262
 30. Glass DR, Tsai AG, Oliveria JP, Hartmann FJ, Kimmey SC, Calderon AA et al (2019) An integrated multi-omic single cell atlas to redefine human B cell memory. *BioRxiv* 226:223–62
 31. Hartmann FJ, Bendall SC (2020) Immune monitoring using mass cytometry and related high-dimensional imaging approaches. *Nat Rev Rheumatol* 16:87–99
 32. Hartmann FJ, Mrdjen D, McCaffrey E, Glass DR, Greenwald NF, Bhargava A et al (2021) Single-cell metabolic profiling of human cytotoxic T cells. *Nat Biotechnol* 39:186–197
 33. Moore AR, Gonzalez NV, Plummer KA, Mitchel OR, Kaur H, Rivera M, et al (2021) Gestationally-dependent immune organization at the maternal-fetal interface. *Biorxiv*
 34. Moen E, Bannon D, Kudo T, Graf W, Covert M, Valen DV (2019) Deep learning for cellular image analysis. *Nat Methods* 16:1233–1246
 35. Greenwald NF, Miller G, Moen E, Kong A, Kagel A, Dougherty T, et al (2021) Whole-cell segmentation of tissue images with human-level performance using large-scale data annotation and deep learning. *Nat Biotechnol* 1–11
 36. Valen DAV, Kudo T, Lane KM, Macklin DN, Quach NT, DeFelice MM et al (2016) Deep learning automates the quantitative analysis of individual cells in live-cell imaging experiments. *PLOS Comput Biol* 12:e1005177
 37. McInnes L, Healy J, Melville J (2018) UMAP: Uniform manifold approximation and projection for dimension reduction. <https://arxiv.org/abs/1802.03426>
 38. Uchihara T (2014) Pretangles and neurofibrillary changes: similarities and differences between AD and CBD based on molecular and morphological evolution. *Neuropathology* 34:571–577
 39. Wang H, Kulas JA, Ferris HA, Hansen SB (2020) Regulation of beta-amyloid production in neurons by astrocyte-derived cholesterol. *Biorxiv*. 62:1495
 40. Calhoun ME, Burgermeister P, Phinney AL, Stalder M, Tolnay M, Wiederhold K-H et al (1999) Neuronal overexpression of mutant amyloid precursor protein results in prominent deposition of cerebrovascular amyloid. *Proc Natl Acad Sci* 96:14088–14093
 41. Zhou L, McInnes J, Wierda K, Holt M, Herrmann AG, Jackson RJ et al (2017) Tau association with synaptic vesicles causes presynaptic dysfunction. *Nat Commun* 8:15295
 42. Heithoff BP, George KK, Phares AN, Zuidhoek IA, Munoz-Ballester C, Robel S (2020) Astrocytes are necessary for blood-brain barrier maintenance in the adult mouse brain. *Biorxiv* 99:125
 43. Liedtke W, Edelmann W, Bieri PL, Chiu F-C, Cowan NJ, Kucherlapati R et al (1996) GFAP is necessary for the integrity of CNS white matter architecture and long-term maintenance of myelination. *Neuron* 17:607–615
 44. Tangalos EG, Petersen RC (2018) Mild cognitive impairment in geriatrics. *Clin Geriatr Med* 34:563–589
 45. Feldman HH, Jacova C (2005) Mild cognitive impairment. *Am J Geriatr Psychiatry* 13:645–655
 46. Rosenberg PB, Lyketsos C (2008) Mild cognitive impairment: searching for the prodrome of Alzheimer's disease. *World Psychiatry* 7:72–78
 47. Lorente-de-Nó R (1934) Studies on the structure of the cerebral cortex II continuation of the study of the ammonic system. *J Psychol Neurol* 46:113–177
 48. Ramón y Cajal S (1902) Fourth-order olfactory areas: Ammon's Horn and the dentate gyrus. In: Press OU (ed). *Histology of the Nervous System: Chapter XXXI II*, pp 603–57
 49. Eriksson PS, Perfilieva E, Björk-Eriksson T, Alborn AM, Nordborg C, Peterson DA et al (1998) Neurogenesis in the adult human hippocampus. *Nat Med* 4:1313–1317
 50. Gassen SV, Callebaut B, Helden MJV, Lambrecht BN, Demeester P, Dhaene T et al (2015) FlowSOM: using self-organizing maps for visualization and interpretation of cytometry data. *Cytom Part A* 87:636–645
 51. Hopperton KE, Mohammad D, Trépanier MO, Giuliano V, Bazinet RP (2018) Markers of microglia in post-mortem brain samples from patients with Alzheimer's disease: a systematic review. *Mol Psychiatry* 23:177–198
 52. Brunello CA, Merezko M, Uronen R-L, Huttunen HJ (2020) Mechanisms of secretion and spreading of pathological tau protein. *Cell Mol Life Sci* 77:1721–1744
 53. Tai H-C, Wang BY, Serrano-Pozo A, Frosch MP, Spire-Jones TL, Hyman BT (2014) Frequent and symmetric deposition of misfolded tau oligomers within presynaptic and postsynaptic terminals in Alzheimer's disease. *Acta Neuropathol Commun* 2:146
 54. Phongprecha T, Gajera CR, Liu CC, Vijayaragavan K, Chang AL, Becker M et al (2021) Single-synapse analyses of Alzheimer's disease implicate pathologic tau DJ1, CD47 and ApoE. *Sci Adv* 7:eabk0473
 55. Corces MR, Shcherbina A, Kundu S, Gloudemans MJ, Frésard L, Granja JM et al (2020) Single-cell epigenomic analyses implicate candidate causal variants at inherited risk loci for Alzheimer's and Parkinson's diseases. *Nat Genet* 52:1158–1168
 56. Motori E, Atanassov I, Kochan SMV, Folz-Donahue K, Sakthivelu V, Gialvalisco P et al (2020) Neuronal metabolic rewiring promotes resilience to neurodegeneration caused by mitochondrial dysfunction. *Sci Adv* 6:eaba8271
 57. Guo T, Zhang D, Zeng Y, Huang TY, Xu H, Zhao Y (2020) Molecular and cellular mechanisms underlying the pathogenesis of Alzheimer's disease. *Mol Neurodegener* 15:40
 58. Li S, Selkoe DJ (2020) A mechanistic hypothesis for the impairment of synaptic plasticity by soluble A β oligomers from Alzheimer's brain. *J Neurochem* 154:583–597
 59. Thomas SN, Funk KE, Wan Y, Liao Z, Davies P, Kuret J et al (2012) Dual modification of Alzheimer's disease PHF-tau protein by lysine methylation and ubiquitylation: a mass spectrometry approach. *Acta Neuropathol* 123:105–117
 60. Sáez ET, Pehar M, Vargas MR, Barbeito L, Maccioni RB (2006) Production of nerve growth factor by β -amyloid-stimulated astrocytes induces p75NTR-dependent tau hyperphosphorylation in cultured hippocampal neurons. *J Neurosci Res* 84:1098–1106
 61. Lemke N, Melis V, Lauer D, Magbagbeolu M, Neumann B, Harrington CR et al (2020) Differential compartmental processing and phosphorylation of pathogenic human tau and native mouse tau in the line 66 model of frontotemporal dementia. *J Biol Chem* 295:18508–18523
 62. Sahara N, Murayama M, Higuchi M, Suhara T, Takashima A (2014) Biochemical distribution of tau protein in synaptosomal fraction of transgenic mice expressing human P301L tau. *Front Neurol* 5:26

63. Quevenec FC, Schreiner SJ, Preti MG, van Bergen JMG, Kirchner T, Wyss M et al (2019) GABA and glutamate moderate beta-amyloid related functional connectivity in cognitively unimpaired old-aged adults. *Neuroimage Clin* 22:101776
64. Wang Z, Jackson RJ, Hong W, Taylor WM, Corbett GT, Moreno A et al (2017) Human brain-derived A β oligomers bind to synapses and disrupt synaptic activity in a manner that requires APP. *J Neurosci* 37:11947–11966
65. Nakayama Y, Sakamoto S, Tsuji K, Ayaki T, Tokunaga F, Ito H (2019) Identification of linear polyubiquitin chain immunoreactivity in tau pathology of Alzheimer's disease. *Neurosci Lett* 703:53–57
66. Arrasate M, Mitra S, Schweitzer ES, Segal MR, Finkbeiner S (2004) Inclusion body formation reduces levels of mutant huntingtin and the risk of neuronal death. *Nature* 431:805–810
67. Mund T, Masuda-Suzukake M, Goedert M, Pelham HR (2018) Ubiquitination of alpha-synuclein filaments by Nedd4 ligases. *PLOS ONE* 13:e0200763
68. Han S, Nandy P, Austria Q, Siedlak SL, Torres S, Fujioka H et al (2020) Mfn2 ablation in the adult mouse hippocampus and cortex causes neuronal death. *Cells* 9:116
69. Sita G, Hrelia P, Graziosi A, Morroni F (2020) Back to the fusion: mitofusin-2 in Alzheimer's disease. *J Clin Medicine* 9:126
70. Wang X, Su B, Lee H, Li X, Perry G, Smith MA et al (2009) Impaired balance of mitochondrial fission and fusion in Alzheimer's disease. *J Neurosci* 29:9090–9103
71. Bendall SC, Davis KL, Amir ED, Tadmor MD, Simonds EF, Chen TJ et al (2014) Single-cell trajectory detection uncovers progression and regulatory coordination in human B cell development. *Cell* 157:714–725
72. Cid E, Marquez-Galera A, Valero M, Gal B, Medeiros DC, Navarron CM et al (2021) Sublayer- and cell-type-specific neurodegenerative transcriptional trajectories in hippocampal sclerosis. *Cell Rep* 35:109229
73. Kimmey SC, Borges L, Baskar R, Bendall SC (2019) Parallel analysis of tri-molecular biosynthesis with cell identity and function in single cells. *Nat Commun* 10:1185
74. Lang C, Campbell KR, Ryan BJ, Carling P, Attar M, Vowles J et al (2019) Single-cell sequencing of iPSC-dopamine neurons reconstructs disease progression and identifies HDAC4 as a regulator of Parkinson cell phenotypes. *Cell Stem Cell* 24:93–106.e6
75. Loeffler-Wirth H, Binder H, Willscher E, Gerber T, Kunz M (2018) Pseudotime dynamics in melanoma single-cell transcriptomes reveals different mechanisms of tumor progression. *Biology* 7:23
76. Weinreb C, Rodriguez-Fraticelli A, Camargo FD, Klein AM (2020) Lineage tracing on transcriptional landscapes links state to fate during differentiation. *Science* 367:3381
77. Gubin MM, Esaulova E, Ward JP, Malkova ON, Runci D, Wong P et al (2018) High-dimensional analysis delineates myeloid and lymphoid compartment remodeling during successful immune-checkpoint cancer therapy. *Cell* 175:1014–1030.e19
78. Chen P, Miah MR, Aschner M (2016) Metals and neurodegeneration. *F1000Research* 5:366–12
79. Livet J, Weissman TA, Kang H, Draft RW, Lu J, Bennis RA et al (2007) Transgenic strategies for combinatorial expression of fluorescent proteins in the nervous system. *Nature* 450:56–62
80. Walker JM, Dehkordi SK, Fracassi A, Vanschoiack A, Pavenko A, Tagliatalata G et al (2022) Differential protein expression in the hippocampi of resilient individuals identified by digital spatial profiling. *Acta Neuropathol Commun* 10:23
81. Prokop S, Miller KR, Labra SR, Pitkin RM, Hoxha K, Narasimhan S et al (2019) Impact of TREM2 risk variants on brain region-specific immune activation and plaque microenvironment in Alzheimer's disease patient brain samples. *Acta Neuropathol* 138:613–630
82. Mostafavi S, Gaiteri C, Sullivan SE, White CC, Tasaki S, Xu J et al (2018) A molecular network of the aging human brain provides insights into the pathology and cognitive decline of Alzheimer's disease. *Nat Neurosci* 21:811–819
83. Johnson ECB, Carter EK, Dammer EB, Duong DM, Gerasimov ES, Liu Y et al (2022) Large-scale deep multi-layer analysis of Alzheimer's disease brain reveals strong proteomic disease-related changes not observed at the RNA level. *Nat Neurosci* 25:213–225
84. Wingo AP, Liu Y, Gerasimov ES, Gockley J, Logsdon BA, Duong DM et al (2021) Integrating human brain proteomes with genome-wide association data implicates new proteins in Alzheimer's disease pathogenesis. *Nat Genet* 53:143–146
85. Montine TJ, Phelps CH, Beach TG, Bigio EH, Cairns NJ, Dickson DW et al (2011) National Institute on Aging–Alzheimer's Association guidelines for the neuropathologic assessment of Alzheimer's disease: a practical approach. *Acta Neuropathol* 123:1–11
86. Bendall SC, Spitzer M, Simonds EF, Nolan GP (2013) Conjugation and characterization of immunoglobulins with stable mass isotope reporters for single-cell mass cytometry analysis, pp 1–29
87. Bosse MM, Bendall S, Angelo M (2021) Metal-antibody MIBitag conjugation kit. protocols.io [Internet]. Available from: <https://protocols.io/view/metal-antibody-mibitag-conjugation-kit-bhyej7te.html>
88. Camacho C, Bosse MM, Bendall S, Angelo M (2021) Antibody lyophilization v1. Protocols.io
89. Bosse MM, Bendall S, Angelo M (2021) MIBI staining V.3. protocols.io [Internet]. Available from: <https://protocols.io/view/mibi-staining-byzrp-x56.html>
90. Bosse MM, Bendall S, Angelo M (2021) IHC staining. protocols.io [Internet]. Available from: <https://protocols.io/view/ihc-staining-bf6ajrae.html>

Publisher's Note

Springer Nature remains neutral with regard to jurisdictional claims in published maps and institutional affiliations.

Ready to submit your research? Choose BMC and benefit from:

- fast, convenient online submission
- thorough peer review by experienced researchers in your field
- rapid publication on acceptance
- support for research data, including large and complex data types
- gold Open Access which fosters wider collaboration and increased citations
- maximum visibility for your research: over 100M website views per year

At BMC, research is always in progress.

Learn more biomedcentral.com/submissions

